Long Wavelength GaInAsP/InP

Semiconductor Lasers for Optical Communications

Thesis by

Chen Pei-Chuang

In Partial Fullfillment of the Requirements

for the degree of

Doctor of Philosophy

California Institute of Technology

Pasadena, California

1982

(Submitted October 9, 1981)

ACKNOWLEDGEMENTS

I wish to express my deep appreciation and sincere gratitude to my advisor, Dr. Amnon Yariv, for his excellent guidance and support throughout the course of this work. It is a privilege to have been a member of his highly motivated quantum electronics group.

Special thanks must go to Dr. Schlomo Margalit and Dr. Nadav Bar-Chaim, without whose inspirational scientific guidance and discussions much of the work involved in this thesis would not have been possible. In addition, I would like to thank Mr. Desmond Armstrong and Mr. Larry Begay for their expert technical assistance in construction and maintenance of experimental apparatus.

I would also like to express my appreciation to my fellow colleagues, Mr. Yu Kit-Lai and Mr. Chiu Liew-Chuang for participation in this work, and Dr. Willie Ng, Dr. C. P. Lee, Dr. Israel Ury, Dr. Daniel Wilt, Dr. Lau Kam-Yin and Mr. Christoph Harder for their many enlightening discussions. And I specially thank Mr. Chiu Liew-Chuang for typing this thesis.

My deepest appreciation goes to my parents and the family of my brother for their love, encouragement and support during these past several years.

And, of course, the secretaries Linda Dozsa, Cindy Gaston, Michelle Schroeder and Jana Mercado have to be mentioned for their exciting friendship and kind assistance during the stay at Caltech.

ABSTRACT

Optical fiber communication systems have shifted toward the long wavelength range of 1.2-1.6 μm due to lower losses and dispersion available with high quality fibers. The quaternary GaInAsP/InP material system has evolved as the most promising system for light sourses in this range.

Indium phosphide electronic devices are expected to possess high frequency switching capabilities, but present device technology is still rather primitive. In anticipation of future developments, which will render opto-electronic integration in this system advantageous, two laser structures on semi-insulating InP substrates were demonstrated. The substrate permits electrical isolation between components and thus is ideal in planar integration of the lasers with electronic devices.

Low threshold lasers can only be achieved when the active region is properly defined in two dimensions to provide good optical and carrier confinement. Present techniques usually require difficult and intricate growth step of two-step liquid phase epitaxy. Embedded epitaxy, by growth through a mask, offers a simple yet elegant means of two dimensional definition of the active region with only a single growth step. Low threshold lasers were fabricated with this technique and demonstrated its potential applications.

All GaInAsP/InP lasers show accelerated increase of threshold current with temperature of a different nature than similar GaAlAs lasers. To understand the origin of this phenomenon, calculations were made of the Auger process in these lasers, and have demonstrated that they play a very important role in the temperature behavior of GaInAsP/InP lasers.

LONG WAVELENGTH GaInAsP/InP SEMICONDUCTOR LASERS FOR OPTICAL COMMUNICATIONS

CONTENTS

page

Chapter 1. INTRODUCTION

1.1 Introduction 1

1.2 Optical Fibers 1

1.3 The Quaternary GaInAsP/InP System 5

1.4 Thesis Outline 7

Chapter 2. GaInAsP/InP LASERS ON SEMI-INSULATING SUBSTRATES

2.1 Introduction 11

2.2 The Crowding Effect 13

2.3 Lasers Based on the Crowding Effect - I
The Crowding Effect Laser 15

2.4 Lasers Based on the Crowding Effect - II
The T-Laser 19

Chapter 3. EMBEDDED EPITAXY AND LOW THRESHOLD EMBEDDED LASERS

3.1 Introduction 26

3.2 Masked Growth and Embedded Epitaxy 28

3.3 Low Threshold Embedded Lasers 37

Chapter 4. INTERBAND AUGER RECOMBINATION IN GaInAsP/InP SEMICONDUCTOR LASERS

4.1 Introduction 51

4.2 Various Mechanisms that Affect
Temperature Threshold Characteristics 53

4.3 The CHCC and CHSH Auger Processes 56

4.4 Comparison of Calculated and Measured Lifetimes 62

Chapter 5. SOME GROWTH AND PROCESSING TECHNIQUES OF GaInAsP/InP DEVICES

5.1 Introduction 75

5.2 LPE of GaInAsP/InP Materials 75

5.3 Device Processing 80

Appendix A: Cleaning and Etching Procedures 87

Appendix B: The Silicon Nitride Deposition System 88

Chapter 1

Introduction

1.1 Introduction

Lightwave communications systems, which send information by encoding it onto light beams propagating in hair-thin glass fibers, are now undergoing rapid development throughout the world. Expected to revolutionize terrestial communication techniques, these systems have been made possible by two technological breakthroughs. The first is the development of glass optical fibers with small optical attenuations. The second is the development of semiconductor light sources for efficiently producing the light which is transmitted in these fibers. A schematic of a basic system is illustrated in Fig. 1.1.

Previous systems envisaged for long distance communications used as a light source a GaAs/GaAlAs double heterostructure laser that emits at about 0.8 μm. However, fibers with extremely low hydro-oxyl ion content have since been made that allow for much lower losses at the longer wavelength region of 1.2-1.6 μm. As a further advantage to go to longer wavelengths, zero total dispersion (material plus waveguide) also exists within this range. Thus, for long distance, high bit-rate data communications, light sources other than those available with the GaAlAs/GaAs material system must be developed. The quaternary GaInAsP/InP system has emerged as the most promising choice.

1.2 Optical Fibers

Two considerations relating to optical fibers are most important in optical transmission systems, i.e., signal attenuation and bandwidth.

Signal attenuation in state of art fibers are mainly attributable to material

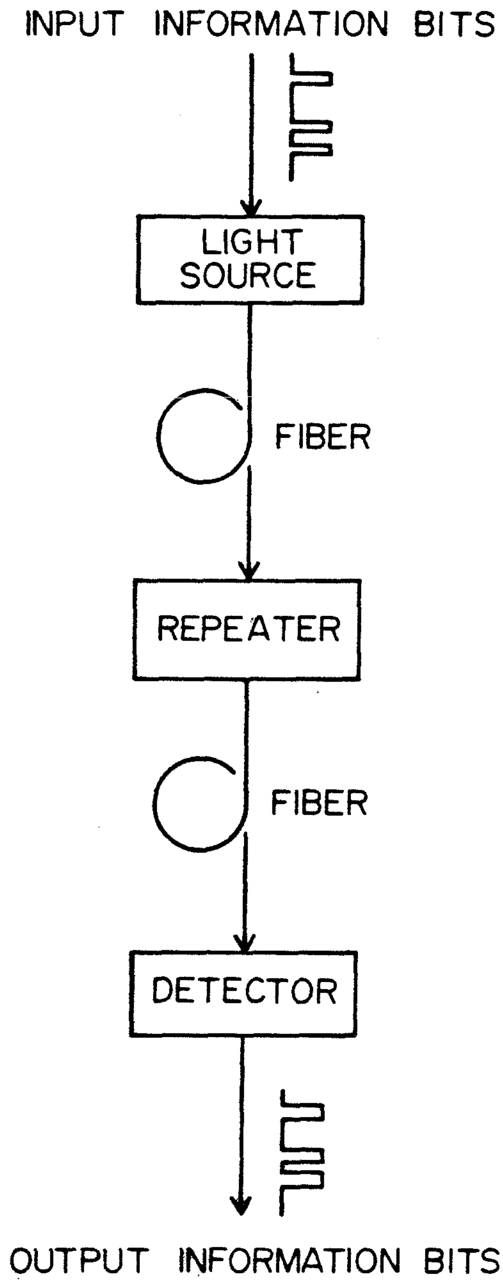

Fig. 1.1 Schematic of optical communiction system.

effects. These include light absorption by impurities such as hydro-oxyl (OH) and transition-metal ions, inherent absorption by the ultraviolet edge of the electronic band and the infrared edge of the vibrational bands of the consistuent glass materials, drawing induced absorption, Rayleigh scattering by refractive index inhomogeneities frozen into the glass lattice, and Mie scattering by foreign inclusions introduced during manufacture. The technology for fiber-preform fabrication has advanced to a level that, basically, only intrinsic effects like Rayleigh scattering and infrared absorption limit the losses. These two factors in effect define the transmission window which extends from 0.7 to 1.8 μm wavelength in current low-loss GeO_2-doped silica fibers. The OH content in these fibers must be kept low, since an impurity level of 1 ppm will give rise to a 30-40 dB/km absorption peak at 1.39 μm [1,2,3]. In some recent fibers, this absorption has almost been totally eliminated. Fig. 1.2 shows the loss spectrum of an ultra-low loss germano-silicate single-mode fiber produced by the MCVD process [4]. Loss components associated with various intrinsic materials effects are also shown. Except for the OH absorption peaks at 0.95, 1.25, and 1.39 μm, the observed loss data follow rather closely the estimated Rayleigh scattering and infrared absorption loss curves.

The bandwidth of a fiber is determined by its structural and physical parameters, as well as its materials properties through chromatic and intermodal dispersion. Chromatic dispersion is the dominant effect that determines the bandwidth of single-mode fibers [5,6] However, birefringence effects due to core ellipticity and strain-induced anisotropy may be the limiting factors at wavelengths where chromatic dispersion is minimum [7].

The specific material dispersion for GeO_2-doped silica passes through zero near $\lambda=1.3\mu m$ [8,9]. It is possible to control the zero-dispersion wavelength in single mode fibers by balancing the (negative) material dispersion against the

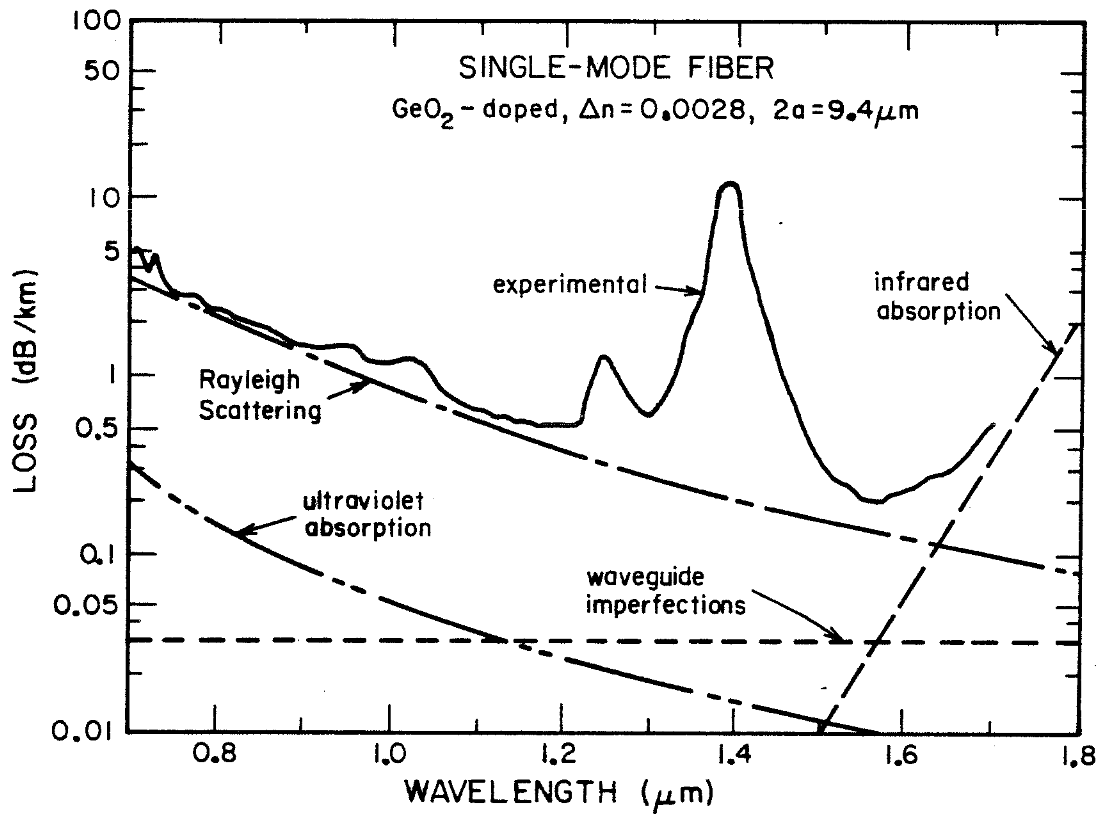

Fig. 1.2 Loss spectrum of a germano-silicate single-mode fiber.

(positive) waveguide dispersion. In this way, the wavelength of minimum dispersion can be shifted to the range where loss is lowest.

1.3 The Quaternary GaInAsP/InP System

In the ternary $Ga_{1-x}Al_xAs$/GaAs system, bandgap of the ternary changes as the amount of Al, x, in the material changes. In this way, direct gap ternary material can be made over the range 0.7 to 0.9 μm. By chance, the lattice constant of the material changes little with composition. Thus, double heterostructure devices with excellent interfacial properties are easily attained [10]. This is critical for low threshold, long-life laser devices.

In contrast, in the long wavelength region of interest, 1.2-1.6 μm, very few other ternary systems enjoy the automatic lattice matching property that GaAlAs/GaAs possesses. However, with the addition of an extra III-V component, exact lattice matching with a given substrate is possible. This extra degree of freedom in quaternary systems has then the advantage of tailoring the desired device wavelength while the condition of exact lattice matching is maintained. The most important quaternary system to date is the $Ga_xIn_{1-x}As_yP_{1-y}$ system [11]. Fig.1.3 shows the entire range that the quaternary GaInAsP covers. It also shows that lattice matched $Ga_xIn_{1-x}As_yP_{1-y}$ on InP spans the range of 0.92-1.65 μm. (In the rest of this thesis, all subscripts will be left out, and it will be understood that all mentioned GaInAsP is lattice matched to InP. The exact composition is determined once the emission wavelength is known.) These lattice matched quaternary materials have smaller bandgaps and higher refractive indices compared with InP. Thus DH structure lasers can be constructed of a quaternary active laser with InP as cladding layers [12]. The fact that both substrate and cladding layers are made of InP introduces some interesting variations in laser structures, in addition to all the well-established structures such as the buried

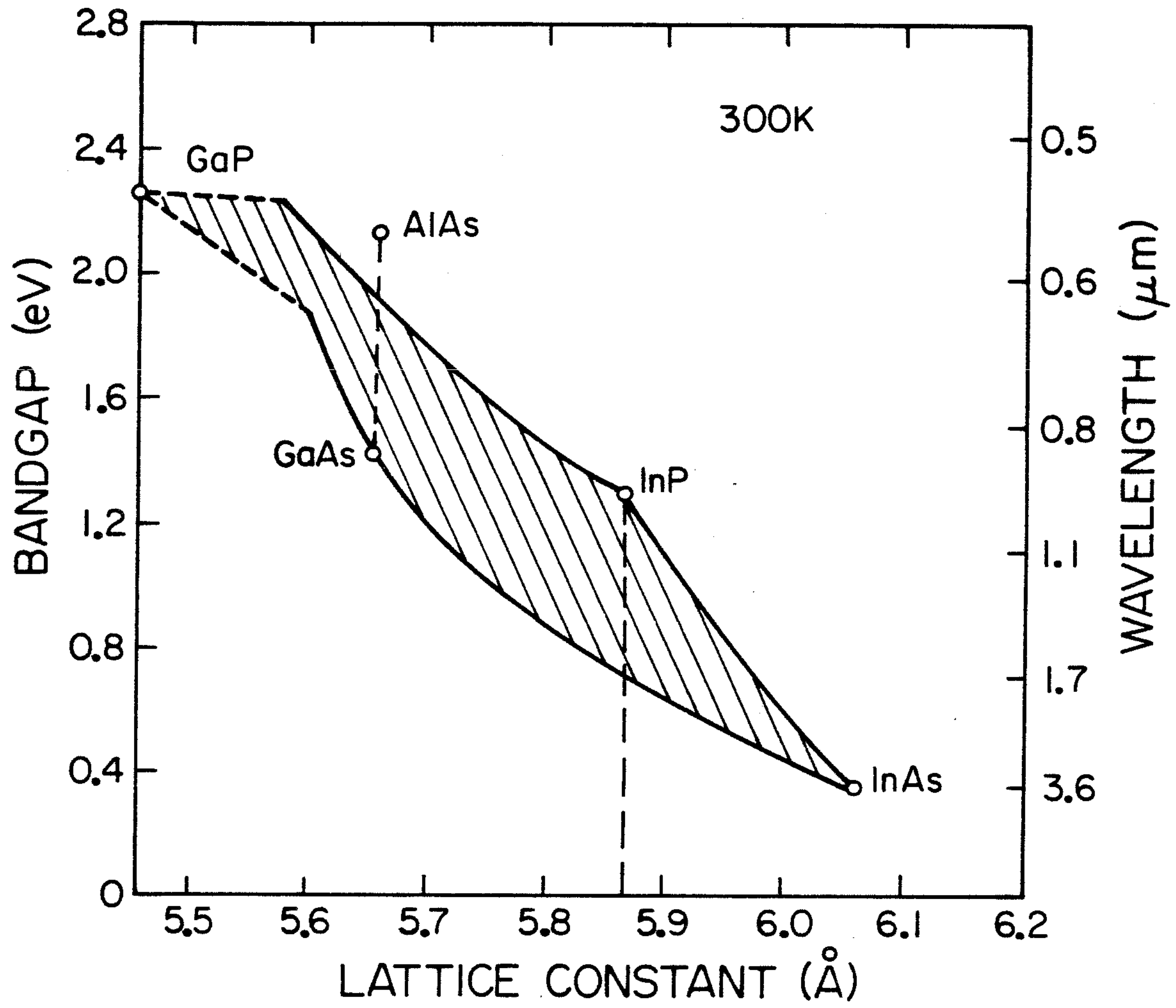

Fig. 1.3 Bandgap vs lattice-constant of the quaternary GaInAsP material system.

heterostructure lasers in the GaAlAs/GaAs system.

Growth of these quaternary materials was at first assumed to be much more difficult than GaAlAs compounds, owing to the complexity involving one extra component. However, even though the physics of the growth is still unclear, good quality materials has been grown without much more effort. In fact, since no aluminum is present in the solution, problems with trace oxygen levels in the growth system are not encountered.

Even though this system did not receive careful attention until recently, the associated technology has advanced at an extremely rapid rate, due in part to much knowledge borrowed from GaAs technology. As a result, many low threshold current lasers have already been fabricated. Reliability of these lasers is currently under intense study. Preliminary results indicate that these devices possess longer life expectancy than their GaAs counterparts at 50°C [13].

1.4 Thesis Outline

Chapter 2 presents work performed on lasers fabricated on semi-insulating InP substrates, which should permit easy integration of electronic devices with lasers. Since integrated optoelectronic devices have been gaining wider attention, these devices should become useful as optical components for integration.

In Chapter 3, a new technique in growth - embedded epitaxy - is introduced. The development of this technique has led to the fabrication of a low threshold current laser with simple processing steps. This technique offers many advantages over the multiple steps required in the fabrication of other state of the art lasers. A detailed description of embedded epitaxy and results of the lasers is presented.

The large dependence of threshold current of the quaternary GaInAsP/InP lasers on temperature has remained a problem. Careful studies to identify the

cause of this large dependence are urgently needed. Chapter 4 presents work in this area. The non-radiative Auger recombination was studied theoretically and compared with experimental data. The results demonstrate that Auger recombination plays an important role in this phenomenon.

Lastly, in Chapter 5, some experimental techniques associated with the growth and fabrication of the GaInAsP/InP DH structures are described.

References - Chapter 1

1. S. E. Miller and A. G. Chynoweth, Eds., **Optical Fiber Telecommunications** , Academic Press, New York (1979)

2. R. Olshansky, "Propagation in Glass Optical Waveguides," Rev. Mod. Phys., **51** , 341(1979)

3. D. B. Keck, R. D. Maurer, and P. C. Schultz, "On the Ultimate Lower-Limit of Attenuation in Glass Optical Waveguides," Appl. Phys. Lett. **22** , 307(1978)

4. T. Miya, Y. Terunuma, T. Hosaka, and T. Miyashita, "Ultimate Low-Loss Single-Mode Fibre at 1.55 μm," Electron. Lett. **15** , 106(1979)

5. D. Marcuse, "Pulse Distortion in Single-Mode Fibers," Appl. Optics. **19** , 1653(1980)

6. W. A. Gambling, H. Matsumara, and C. M. Ragdale, "Mode Dispersion, Material Dispersion and Profile Dispersion in Graded-Index Single-Mode Fibers," Microwaves, Opt. Acoust., **3** , 239(1979)

7. H. Tsuchiya, and N. Imoto, "Dispersion-Free Single-Mode Fiber in 1.5 μm Wavelength Region," Electron. Lett. **15** , 476(1979)

8. D. N. Payne, and W. A. Gambling, "Zero Material Dispersion in Optical Fibers," Electron. Lett. **11** , 176(1975)

9. L. G. Cohen, and C. Lin, "Pulse Delay Measurements in the Zero Material Dispersion Wavelength Region for Optical Fibers," Appl. Opt. **12** , 3136(1977)

10. H. C. Casey, Jr. and M. B. Panish, **Heterostructure Lasers: Part B ,Materials and Operating Characteristics** , Academic Press, New York (1978)

11. R. L. Moon, G. A. Antypas, and L. W. James, "Bandgap and Lattice Constants of GaInAsP as a Function of Alloy Composition," J. Electron Mater., **3** , 635(1974)

12. J. J. Hsieh, "Room-Temperature Operation of GaInAsP/InP Double Heterostructure Diode Lasers Emitting at 1.1 μm," Appl. Phys. Lett. **28** , 283(1976)

13. M. Takusagawa, "Long-Wavelength Lasers," Paper **TUA1** , Int. Conf. on Integrated Opt. and Optical Fiber Commun., San Fran., April(1981)

Chapter 2

GaInAsP/InP Lasers on Semi-Insulating Substrates

2.1 Introduction

It has been pointed out by Yariv [1] that since both high speed electronic devices and excellent quality optical devices can be made from semiconductor materials such as GaAs, it would be advantageous to integrate the two components monolithically on the same substrate. These optoelectronic devices may serve in data communication systems as transmitters, repeaters and receivers. Some Optoelectronic Integration Circuits (OEIC) have already been fabricated in the GaAlAs/GaAs system [2-4]. An example of an integrated transmitter consisting of a metal-semiconductor field effect transistor (MESFET) and a laser is shown in Fig. 2.1.

It is interesting to speculate on the feasibility and possible advantages of such an integration in the InP based system. Microwave devices such as transferred-electron amplifiers and Schottky field effect transistors (FET) have already been developed since 1970. Recently both normally-on (depletion mode) [5] and normally-off (enhancement or inversion mode) [6] InP metal-insulator semiconductor FET (MISFET) devices have been developed. Compared to alternative gating mechanisms such as Schottky and heterojunction structures, an insulated gate allows for large positive and negative input voltage excursions limited only by the stability of the dielectric. Such bipolar operation enhances the dynamic range of the device, which in turn permits for larger signal, and thus, power handling capability. While GaAs MISFETs exhibit excellent high frequency characteristics, their low frequency response is invariably inferior due to the high density of states at the GaAs/insulator interface [7]. This problem of reduced low frequency response is also present in InP MISFETs but to a much smaller degree [8]. Furthermore, it is expected that FET's fabricated on a

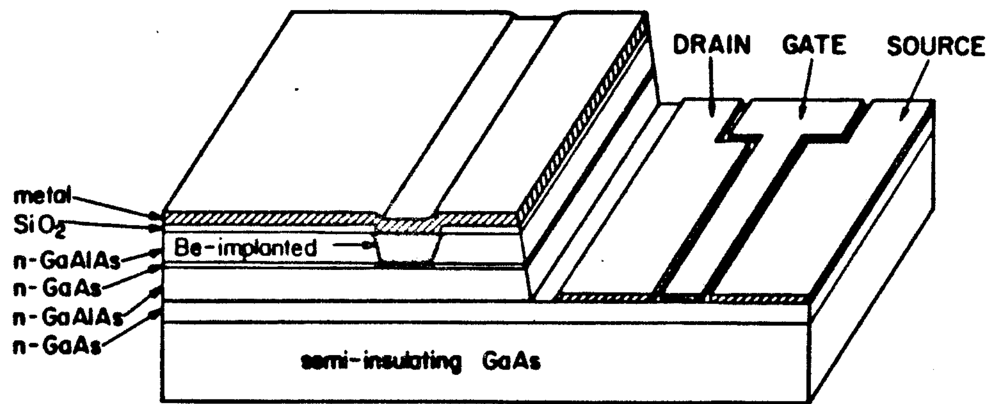

Fig. 2.1 An integrated MESFET/Laser in the GaAlAs/GaAs system.

GaInAs layer lattice matched to InP are capable of even higher speed than GaAs or InP FET's because of a larger peak electron velocity [9]. Since lattice matched GaInAsP on InP double heterostructure (DH) lasers capable of high speed modulation are already technologically available, optoelectronic integration in the GaInAsP/InP system could be potentially as important as, and perhaps even more advantageous than GaAs based ones.

For such an integration to be effective, individual components should be electrically isolated, and parasitic resistance must be reduced. Since high quality semi-insulating InP substrates with resistivities of about 10^7 Ω-cm are commercially available, it would be natural to fabricate all devices on these substrates. Towards this end, lasers on semi-insulating substrates that can be contacted laterally are needed.

The lasers developed here for this purpose are grown by liquid phase epitaxy on Fe-doped semi-insulating InP substrates. Problems associated with thermal conversion do not plaque these substrates, as do Cr-doped GaAs ones [10]. These lasers operate under the principle of the crowding effect.

2.2 The Crowding Effect

Fig. 2.2 shows a structure based on the crowding effect. Current from the n-contact pad travels towards the p-contact through the n-InP layer. Owing to the high sheet resistance of this layer, the potential difference across the pn junction decreases with distance from the edge of the step. This causes the injected current to cross the pn junction close to the step edge. A laser with such a structure will have its optical gain limited to a small region, the size of which is governed by the resistivity of the n-layer. Analysis of the crowding effect has been performed by Lee et al [11]. The results show that the current crossing the pn junction $j_y(x)$ varies as

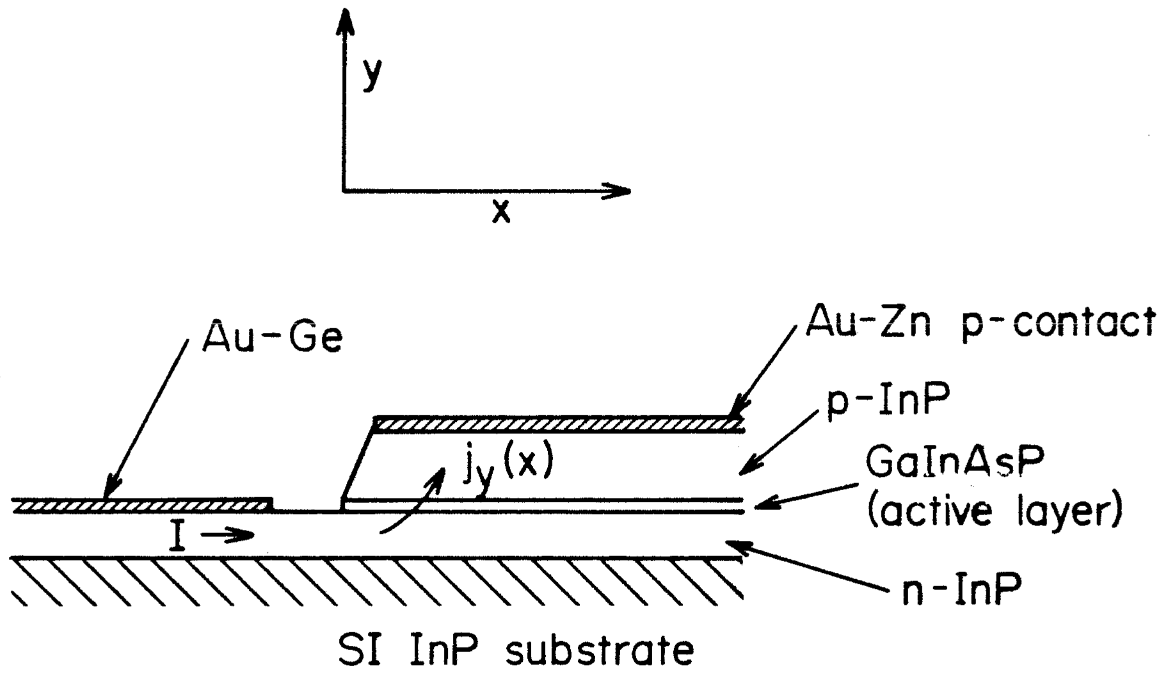

Fig. 2.2 Structure of the Crowding Effect Laser.

$$j_y(x) = \frac{\sqrt{2}\, I}{x_o(\frac{x}{x_o}+\sqrt{2})^2 L} \qquad (2.1)$$

where x is the distance along the n-layer measured from the mesa edge. x_o is given by

$$x_o = \frac{\sqrt{2} mkTL}{eRI} \qquad (2.2)$$

Here L is the length of the laser, R the sheet resistance of the n-layer, k the Boltzman constant, T is the absolute temperature, m lies between 1 and 2, e is the electronic charge. A plot of $\frac{j_y(x)}{j_y(0)}$ vs $\frac{x}{x_o}$ is given in Fig. 2.3. For typical devices, with operating current I=200 mA, L=300 μm, n=8×10^{17}cm^{-3}, x_o is about 3 μm at room temperature.

2.3 Lasers Based on the Crowding Effect - I

The Crowding Effect Laser

The simplest laser based on the above principle is the crowding effect laser (CEL) [11] which was demonstrated in the GaAlAs/GaAs system. However, fabrication of such a structure in the quaternary GaInAsP/InP system has not been attempted, nor any other structure on semi-insulating InP substrates. In our work, the lasers were grown by two-phase liquid phase epitaxy using standard sliding boat technique. A polished (100) semi-insulating InP substrate was first cleaned in acetone and propanol to remove organic contaminants. After rinsing in de-ionized water, the substrate was placed in concentrated nitric acid for five minutes and then rinsed thoroughly in de-ionized water. Just prior to loading into the growth system with all the other necessary dopants and constituents,

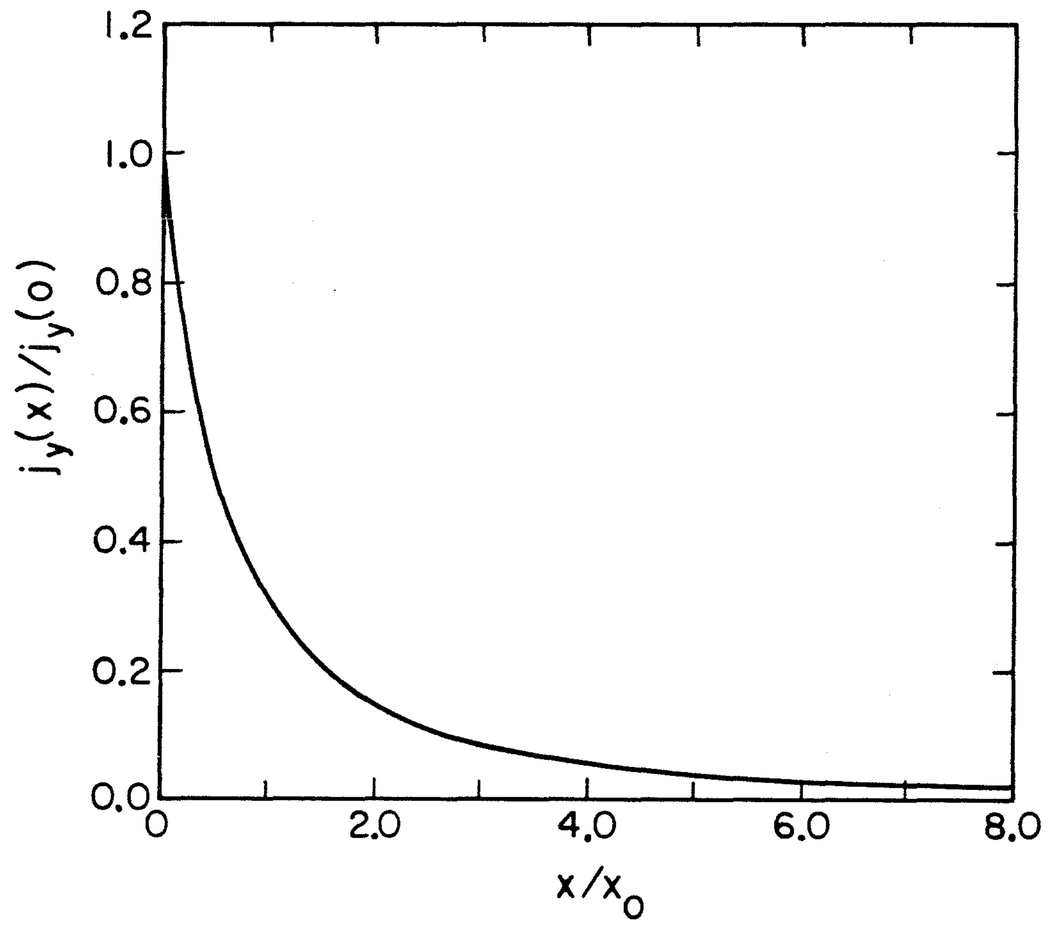

Fig. 2.3 Junction current vs crowding distance x in a CEL.

the substrate was etched in 1% Br-Methanol for three minutes to take off a few μm from the top surface.

Indium for the growth solution was etched in nitric acid for two minutes, then rinsed in de-ionized water and blown dry with dry nitrogen. It was placed in the boat and baked at 730°C for ten hours in palladium-purified hydrogen. The cleaned substrate, dopants and saturation wafers were then loaded. After flushing with purified hydrogen for a few hours, the furnace was heated to 675 °C for one hour to allow the solutions to equilibriate. A cooling ramp in temperature of 0.7 °C/min was then established. The substrate was placed under a pure indium back etch solution for ten seconds to remove the top thermal damaged layer. This ensured a clean, smooth surface for subsequent epilayer growths. Three layers, consisting of a tin doped ($n \sim 8 \times 10^{17} cm^{-3}$) InP, an undoped GaInAsP and a zinc doped ($p \sim 2 \times 10^{18} cm^{-3}$) InP were successively grown. The thicknesses were 1 μm, 0.7 μm and 1.5 μm respectively for the n, quaternary and p layers.

After growth, Au-Zn was evaporated all over the wafer. Shipley AZ 1350B photoresist was then spun on, and half side of this was exposed under ultraviolet light and developed away. Au etch, $HCl:H_2O$ (4:1) and $H_2SO_4:H_2O_2:H_2O$ (3:1:1) were used to etch away the Au-Zn, p-InP and quaternary layers respectively on the exposed side. The photoresist was removed and alloying of the Au-Zn contact was effected at 420 °C for ten seconds. Au-Ge, the contact metal to the bottom n-layer, was selectively evaporated and alloyed at 280 °C for thirty seconds. The wafer was lapped down to 75 μm and cleaved into bars of about 300 μm widths, which were then tested with 100 nsec pulses for lasing. Fig 2.2 shows a sketch of the final structure.

Threshold currents of about 250-300 mA were found for these lasers. These values are encouraging considering the simplicity of this structure. A plot of the L-I characteristics of such a laser is shown in Fig. 2.4. Light output is linear and

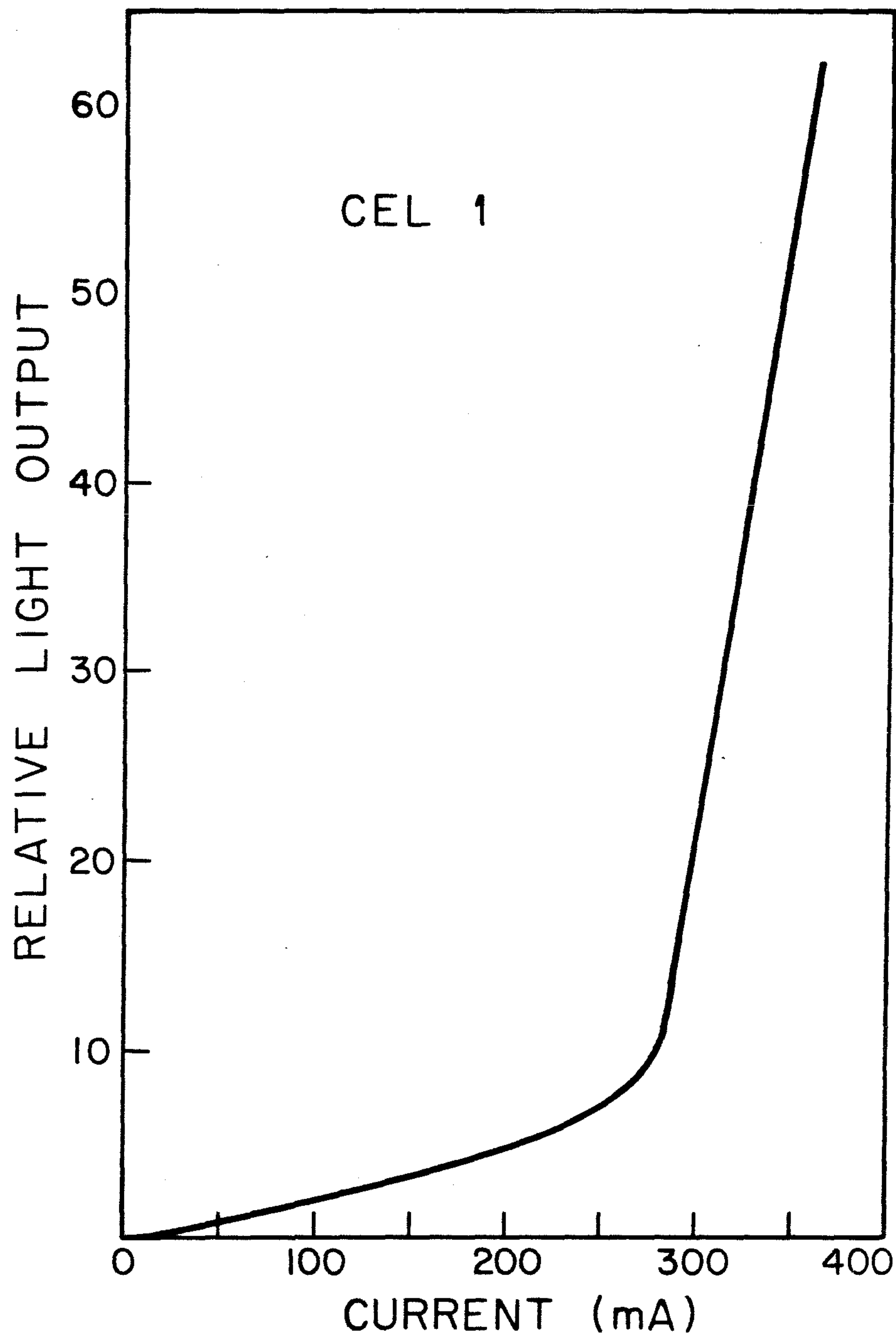

Fig. 2.4 L-I characteristic of a CEL.

kinks are typically absent up to twice threshold.

The threshold current of this structure was relatively high because much current crossed the pn junction away from the lasing region. In addition, real index optical guiding was provided on one side only by the air-crystal interface at the step, while the rest arose from gain guiding. Lower thresholds would be possible if better carrier confinement and optical guiding were provided.

2.4 Lasers Based on the Crowding Effect - II

The T-Laser

With these considerations in mind, the T-laser was proposed and fabricated. The structure and processing (Fig. 2.5) were similar to the CEL except that a narrow mesa instead of a step was formed by the lithography and etching step. Contact to the mesa was made possible by an adjoining T-bridge to a large contact-pad, from which the name of the laser was derived. Distance from the mesa to the contact pad was 2 mm so that current crossing the pn junction under the contact pad was minimal because of the high sheet resistivity of the bottom n-InP layer. Thresholds were 150-200 mA for lasers of 25 μm stripe width, and 100-150 mA for those with 10 μm stripe width, with the lowest value of 95 mA for a 300 μm long laser with a 10 μm stripe. Kinkless light output was obtained (Fig. 2.6) while measured differential quantum efficiency was about 35% from both facets.

An oxide-stripe laser with the same stripe width would have a much higher threshold current due to current spreading. In a mesa-stripe structure as in the T-laser, little or no current is lost outside the active region. Surface recombination of carriers at the sidewalls of the active layer may increase the threshold current density, although this is not expected to affect GaInAsP/InP lasers

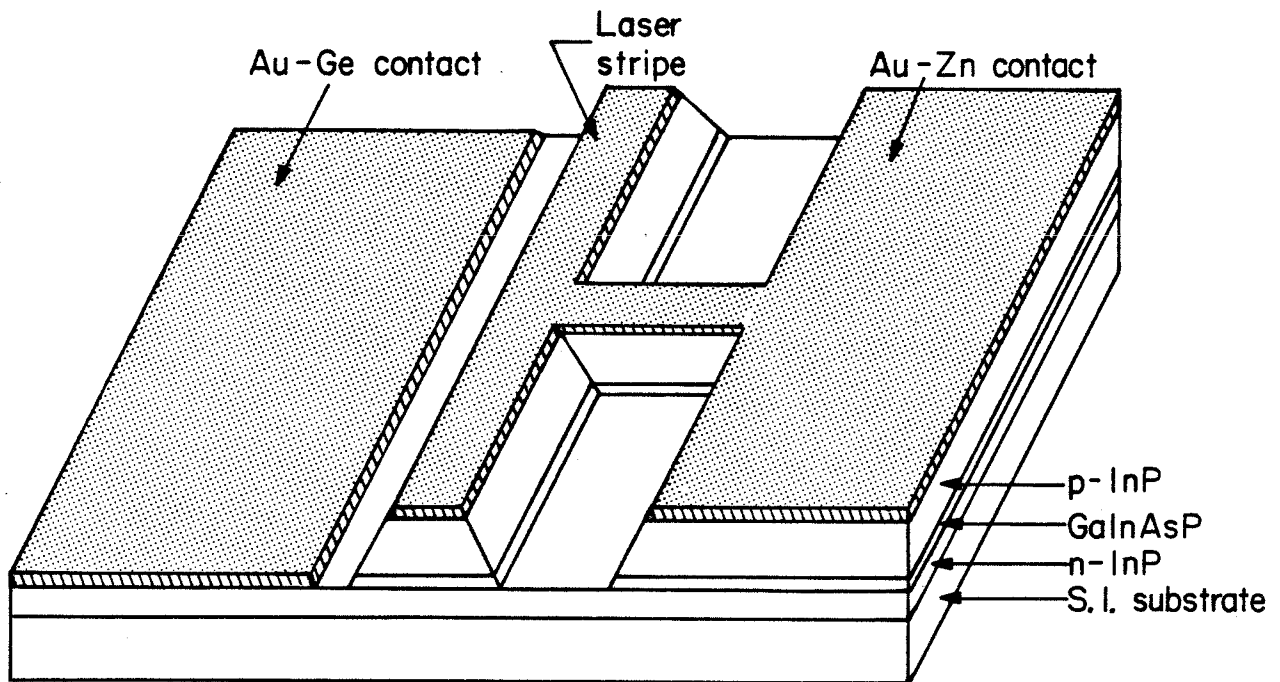

Fig. 2.5 Structure of a T-Laser

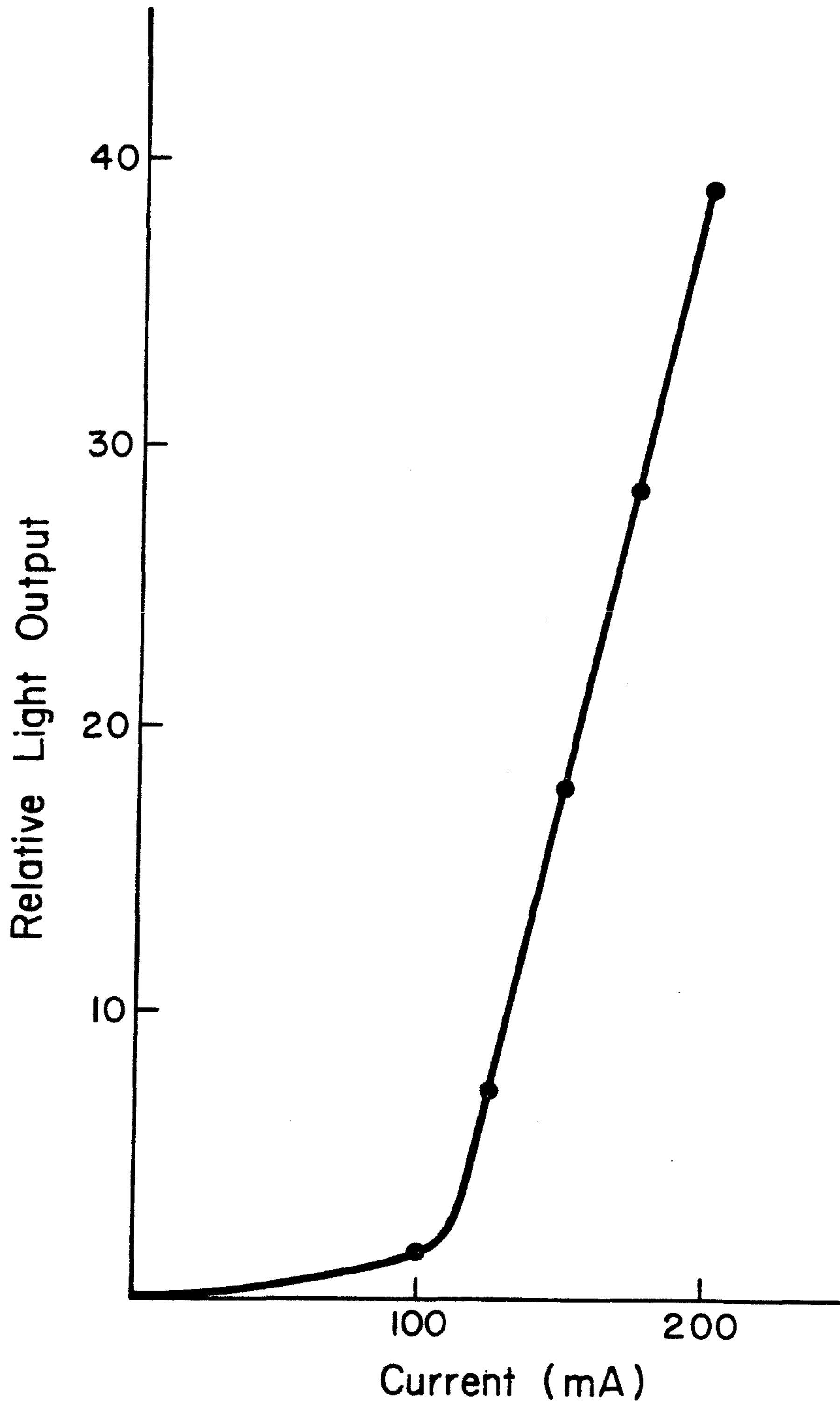

Fig. 2.6 L-I characteristic of a T-Laser.

drastically due to the low surface recombination velocity (almost ten times slower than in GaAs). The major contribution to higher J_{th} in narrower stripe-width mesa lasers probably arises from increased effect of scattering losses at the rough sidewalls. Selection of a smoother etchant would improve the threshold current even more.

The present results already compare favorably with similar devices made on GaAs even though broad area threshold current densities were typically lower in GaAlAs/GaAs Double Heterostructure lasers. This may in part be due to lower surface recombination velocities of carriers in InP and GaInAsP compared to GaAs.

A lasing spectrum for a 10 μm laser is shown in Fig. 2.7. These lasers typically operate in a single longitudinal mode below 1.2 I_{th}, above which, only a few longitudinal modes predominate.

In conclusion, we have demonstrated the first GaInAsP/InP DH lasers on semi-insulating substrate which are compatible with opto-electronic integration.

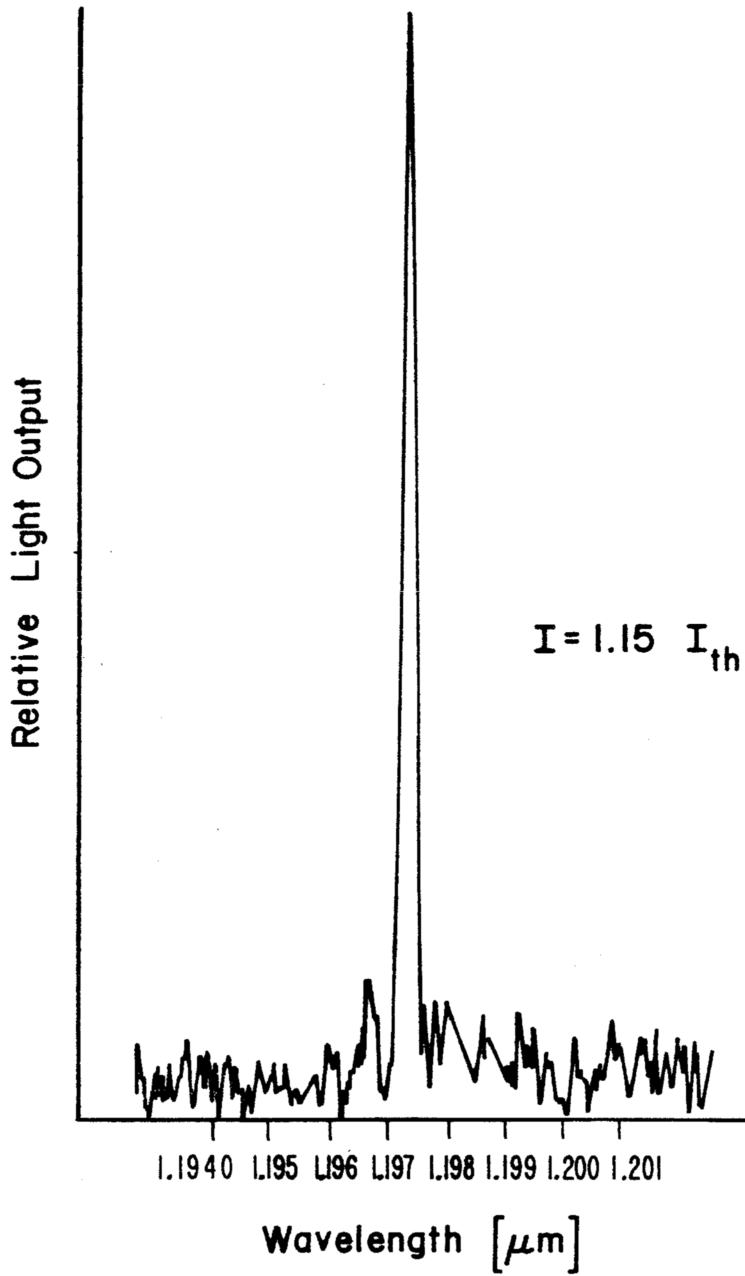

Fig. 2.7 Spectrum of a T-Laser.

References - Chapter 2

1. A. Yariv, "Active Integrated Optics," Proc. Esfahan Symposium on Fundamental and Applied Laser Physics, M. S. Feld, A. Javan, and N. A. Kurnit, eds., Wiley-Interscience, New York (1973)

2. C. P. Lee, S. Margalit, I. Ury, and A. Yariv, "Integration of an Injection Laser with a Gunn Oscillator on a Semi-Insulating GaAs Substrate," Appl. Phys. Lett. **32** , 806(1978)

3. I. Ury, S. Margalit, M. Yust, and A. Yariv, "Monolithic Integration of an Injection Laser and a Metal-Semiconductor Field Effect Transistor," Appl. Phys. Lett. **34** , 430(1979)

4. M. Yust, N. Bar-Chaim, S. H. Izadpanah, S. Margalit, I. Ury, D. Wilt, and A. Yariv, "A Monolithic Integrated Optical Repeater," Appl. Phys. Lett. **35** , 795(1979)

5. L. Messick, D. L. Lile, and A. R. Clawson, "A Microwave InP/SiO_2 MISFET," Appl. Phys. Lett. **32** , 494(1978)

6. D. L. Lile, D. A. Collins, L. G. Meiners, and L. Messick, "n-Channel Inversion-Mode InP MISFET," Electron. Lett. **14** , 657(1978)

7. D. L. Lile, D. A. Collins, L. Messick, and A. R. Clawson, "A Microwave GaAs Insulated Gate FET," Appl. Phys. Lett. **32** , 247(1978)

8. L. Messick, "A D.C. to 16 GHz Indium Phosphide MISFET," Sol. St. Electron. **23** , 551(1980)

9. A. Cappy, B Chanez, R. Fauguembergues, G. Salmer, and E. Constant, " Comparative Potential Performance of Si, GaAs,, GaInAs, InAs Submicrometer-Gate FET's," IEEE Trans. Electron Devices, **ED-27** , 2158(1980)

10. C. A. Evans, V. R. Deline, T. W. Sigmon, and A. Lidow, "Redistribution of Cr Dur-

ing Annealing of ^{80}Se-Implanted GaAs," Appl. Phys. Lett. **35** , 291(1979)

11. C. P. Lee, S. Margalit, and A. Yariv, 'Double Heterostructure GaAs-GaAlAs Lasers on Semi-Insulating Substrates Using Carrier Crowding," Appl. Phys. Lett. **31** , 281(1977)

Chapter 3

Embedded Epitaxy and Low Threshold Embedded Lasers

3.1 Introduction

In optical applications, semiconductor lasers with low thresholds are desirable. It is well understood that structure-wise, low thresholds are achieved when there exists good optical, current and carrier confinement [1]. Optical gain, which depends on the size of overlap of the optical mode with the carrier distribution, is high in such structures. An active region which is surrounded on all sides by claddings with higher bandgaps and lower refractive indices satisfies such criteria if current is limited to this region. The differences in barrier heights prevent carriers injected into the active region from escaping, while real index guiding of the optical mode is provided through the index steps.

The most successful laser structure to date with these properties has been the buried heterostructure laser [2,3]. Basic processing steps, illustrated in Fig. 3.1, involve an initial 3-layer growth of n-InP, quaternary GaInAsP and p-InP on an n-InP substrate. A mesa is chemically etched in the wafer employing a SiO_2 mask, which is also used as a growth mask in a regrowth step when reverse biased junctions are formed on the areas outside the mesa. The growth mask is removed and a new layer of SiO_2 is deposited. The p-contact to the mesa top is then formed by a shallow Zinc-diffusion through an opening. Due to the reverse biased junctions on the sides, current is restricted mainly to pass through the active region. Although this structure produces good quality lasers with low thresholds, with about $I_{th} \sim$ 10 mA per μm of active region width, the numerous difficult steps involved in the processing renders the yield low. Furthermore, any uneveness along the mesa walls resulting from the chemical etching acts as a scattering center that manifests as side lobes in the far field pattern of the

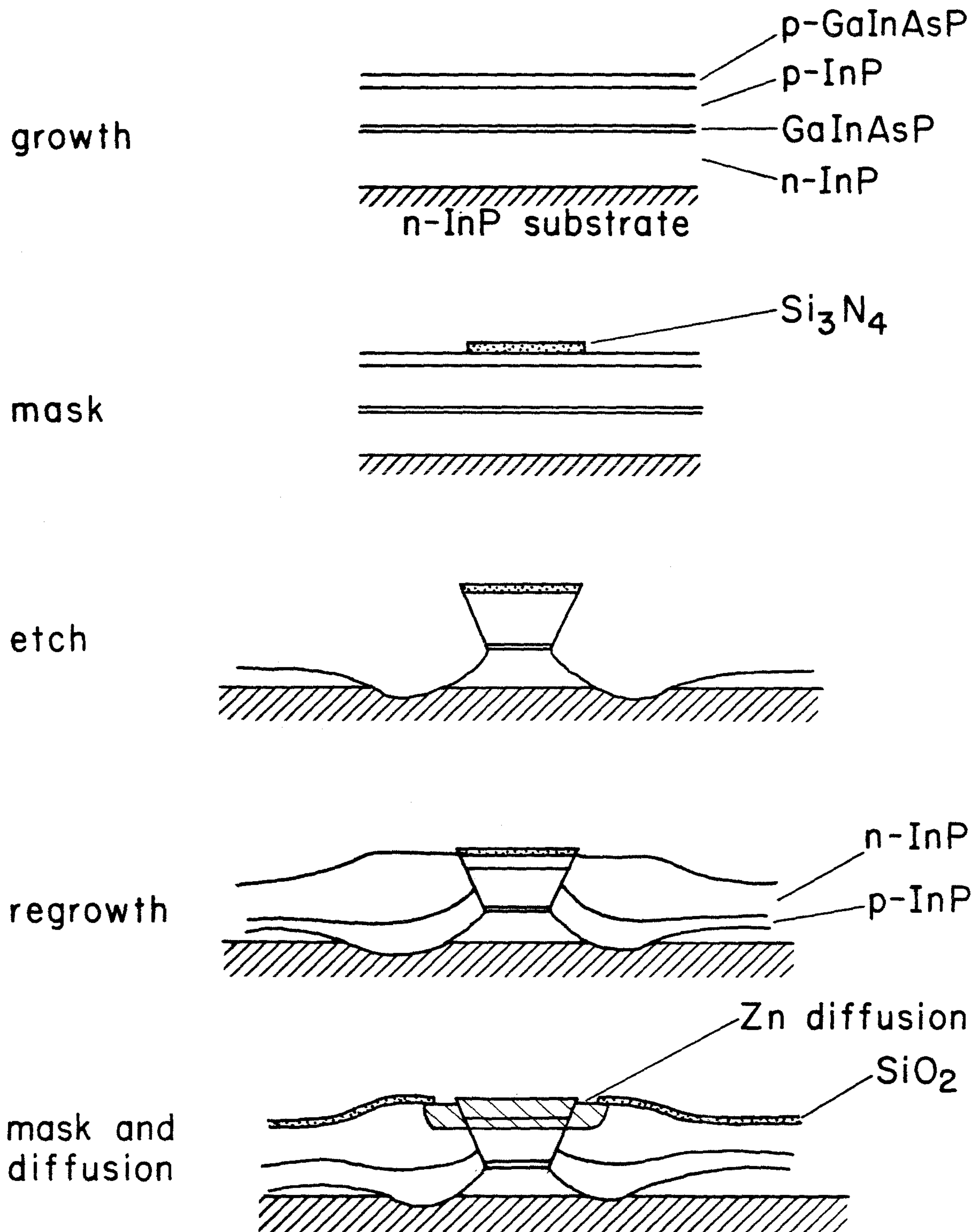

Fig. 3.1 Processing steps for a BH Laser.

laser.

An attractive alternative of obtaining strong carrier and optical confinement is through the technique of embedded epitaxy [4]. In this application, the substrate is covered with a thin layer of dielectric everywhere except for areas where growth is desired. During growth of multilayers, each successive layer almost completely covers over the previous one. A typical three layer growth on a stripe will have the middle layer completely embedded by the first and third layers, thus the name "embedded epitaxy". This method has been applied to GaAlAs/GaAs epitaxy and resulted in low threshold current densities, but difficulty was encountered in attempts at reducing the active layer stripe width that prevented the fabrication of low threshold current lasers [5]. As will be discussed later, this difficulty has been completely eliminated by a simple modification of the technique. This later also led to the successful fabrication of very low threshold GaAlAs/GaAs lasers [6]. The necessary steps are shown in Fig. 3.2 as a comparison with the BH lasers. The simplicity in processing is easily discerned.

3.2 Masked Growth and Embedded Epitaxy

Since no prior study in masked growth was available for the quaternary system, we first sought to characterize this process. A thin silicon nitride dielectric film of 1000 Å was deposited onto a pre-cleaned n-InP substrate as described in chapter 5. 20 μm lines were opened in either the [011] or [01$\bar{1}$] directions. Three successive layers were then deposited. For growth on [011] channels, the growth rate on the (100) facet was faster than on the (111) facets, while the reverse was true for layers deposited on [01$\bar{1}$] channels. From the cross sections (Fig. 3.3), it is seen that the middle quaternary layer is completely embedded within the top and bottom confining InP layers. These structures should lase with thres-

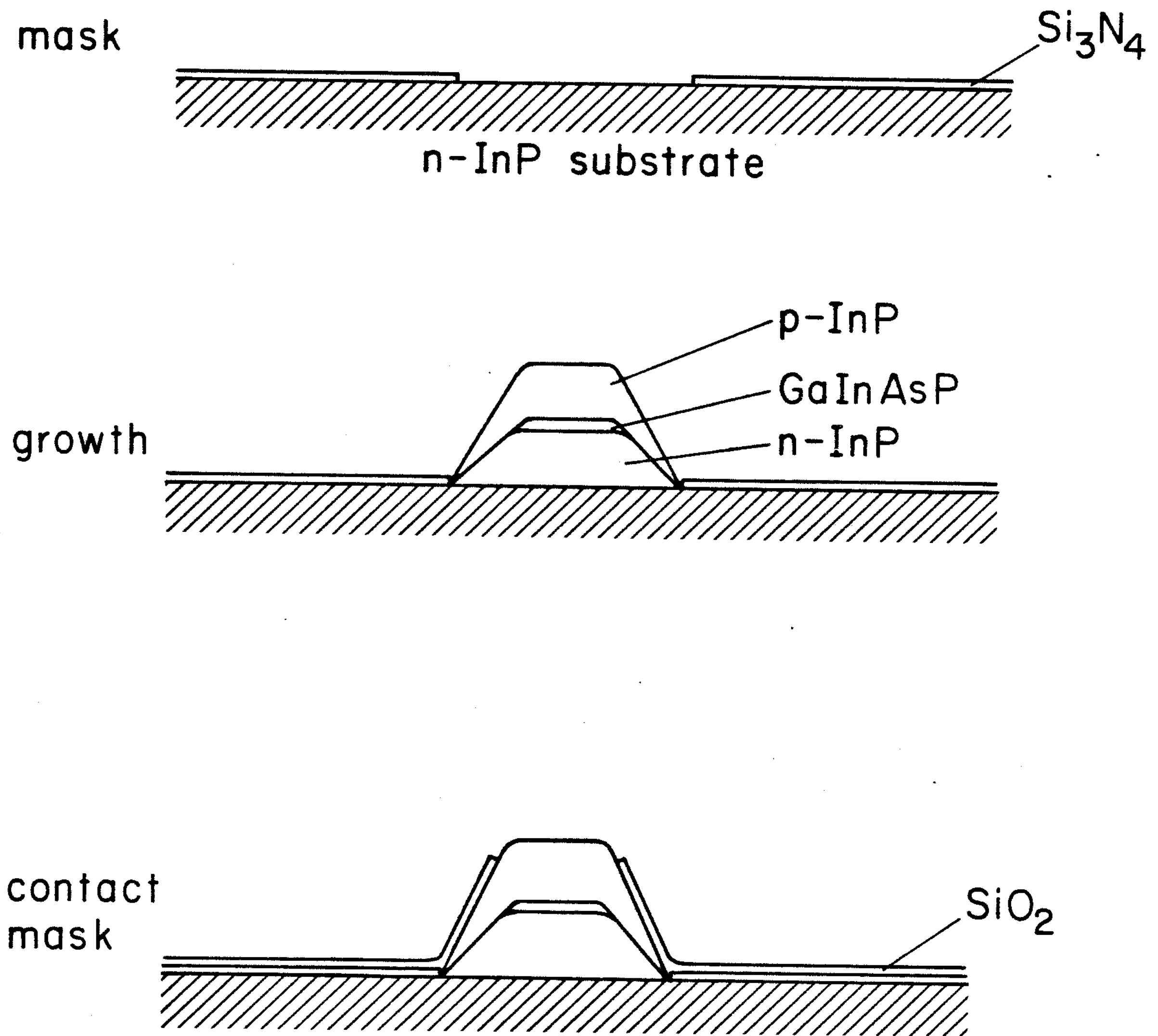

Fig. 3.2 Processing steps for an Embedded Laser.

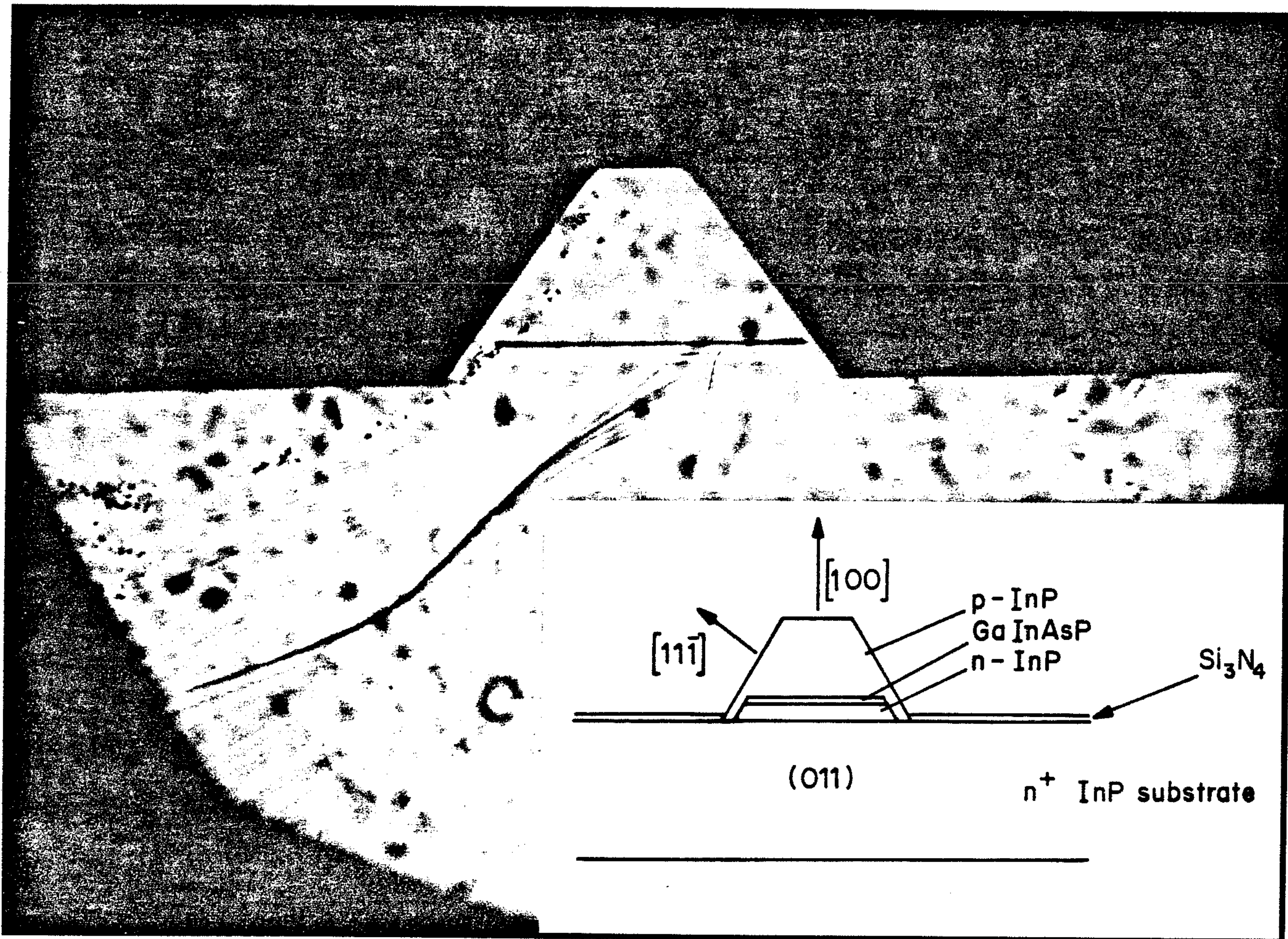

Fig. 3.3a Growth of a DH structure on a 20 μm stripe along [011] direction.

Inset shows schematic of structure.

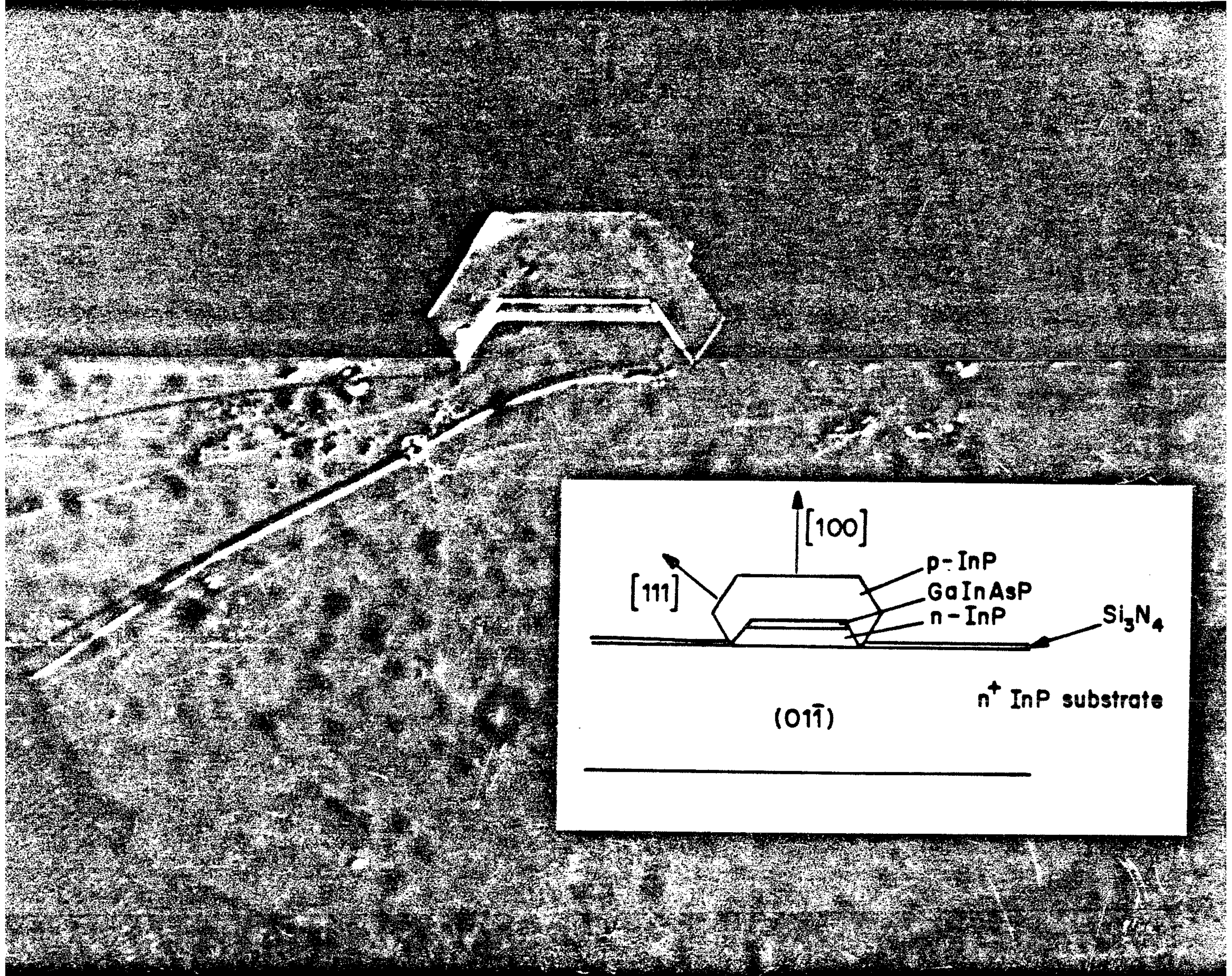

Fig. 3.3b Growth of a DH structure on a 20 μm stripe along [01$\bar{1}$] direction.

Inset shows schematic of structure.

hold current densities comparable to those of conventional BH lasers. To achieve low threshold currents, however, it is necessary to decrease the active region width, while keeping its thickness at ~ 0.2 μm.

Similar to GaAlAs/GaAs growths, it was found that the growth rate increased rapidly as the stripe width was reduced [4], rendering the deposition of thin layers extremely difficult. This was the result of having the excess solute crystallize over a small area.

To understand this problem, we have examined the growth using a diffusion-limited model, i.e., growth depends only on how fast the solute diffuses towards the growth surface. The equation that governs this is

$$\nabla^2 C = \frac{1}{D}\frac{\partial C}{\partial t} \tag{3.1}$$

where $C(x,y,z,t)$ is the concentration of the solute, phosphorous in this case, and D is its diffusion constant. For growth over stripes, this reduces to two dimensions

$$D\left(\frac{\partial^2 C}{\partial x^2}+\frac{\partial^2 C}{\partial z^2}\right) = \frac{\partial C}{\partial t} \tag{3.2}$$

where the substrate is on the $z=0$ plane. For step-cooled growth, the solution is saturated at temperature T_o, and thereafter brought into contact with the substrate at a lower temperature T_1. The concentrations of solute that is in equilibrium with temperatures T_o and T_1 are C_o and C_1 respectively (Fig. 3.4). Initial conditions that exist can be stated as

$$C(x,z,0) = C_o \qquad z > 0 \tag{3.3}$$

If the stripe opening is between $-\frac{w}{2} < x < \frac{w}{2}$, then the necessary boundary conditions are

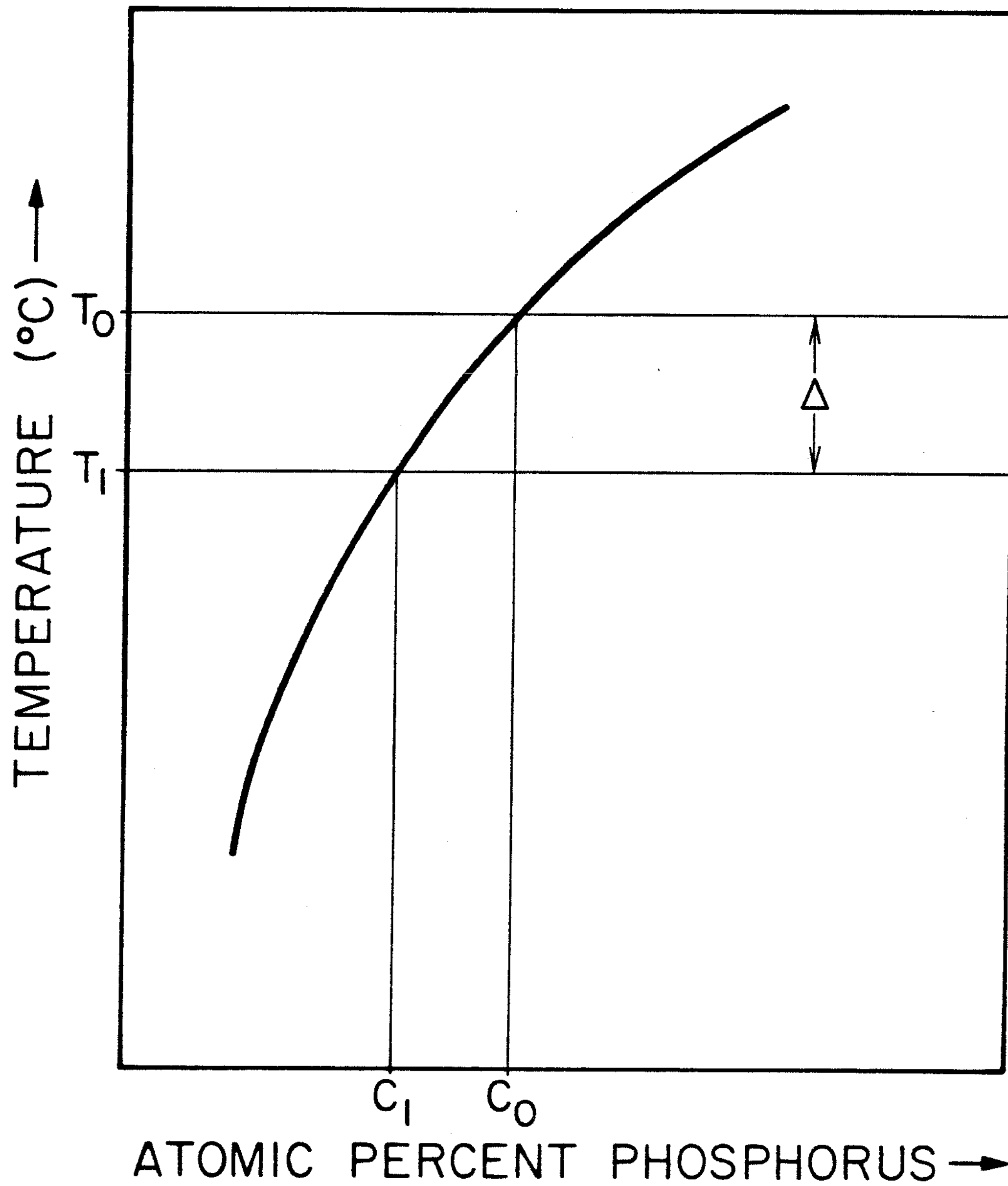

Fig. 3.4 Solidus curve for phosphorus illustrating growth mechanism of LPE.

$$D\frac{\partial C}{\partial z}(z=0) = \frac{\partial P}{\partial t} \qquad -\frac{w}{2} < x < \frac{w}{2} \qquad (3.4a)$$

$$C(x,0,t) = C_1 \qquad -\frac{w}{2} < x < \frac{w}{2} \qquad (3.4b)$$

$$D\frac{\partial C}{\partial z}(z=0) = 0 \qquad |x| \geq \frac{w}{2} \qquad (3.4c)$$

Here P is the amount of solute deposited.

One limiting case is immediately solvable, by letting $w \rightarrow \infty$, when the problem is one-dimensional. The solution is well known [7],

$$P = 2(C_o - C_1)\sqrt{\frac{Dt}{\pi}} \qquad (3.5)$$

The deposition rate of the limit when $w \rightarrow 0$ can also be immediately recognized as illustrated pictorially in Fig. 3.5. Within time t, all solutes within a radius of $\sqrt{Dt}$ have time to reach the stripe. Thus in this case, P is proportional to the area of the semicircle of radius $\sqrt{Dt}$, i.e., proportional to Dt.

For intermediate cases, the solution cannot be obtained analytically, and a finite difference numerical method was applied to solve this problem on a computer. The mole fraction of phosphorus dissolved in the liquid phase at temperature T is given by [8]

$$C = 1.76 \times 10^3 \exp\left(\frac{-11411}{T}\right) \qquad (3.6)$$

and the diffusion constant is taken to be [9] $D = 1.2 \times 10^{-5} cm^2/sec$. The results for a step-cooling of 5°C at 650°C are shown in Fig. 3.6. It shows that thin layers ($\sim 0.2\ \mu m$) cannot be obtained for reasonable growth times when the stripe width is small. Some experimental points for 20 μm stripes grown in the presence of a 0.7°C/min cooling ramp are also plotted on the same graph.

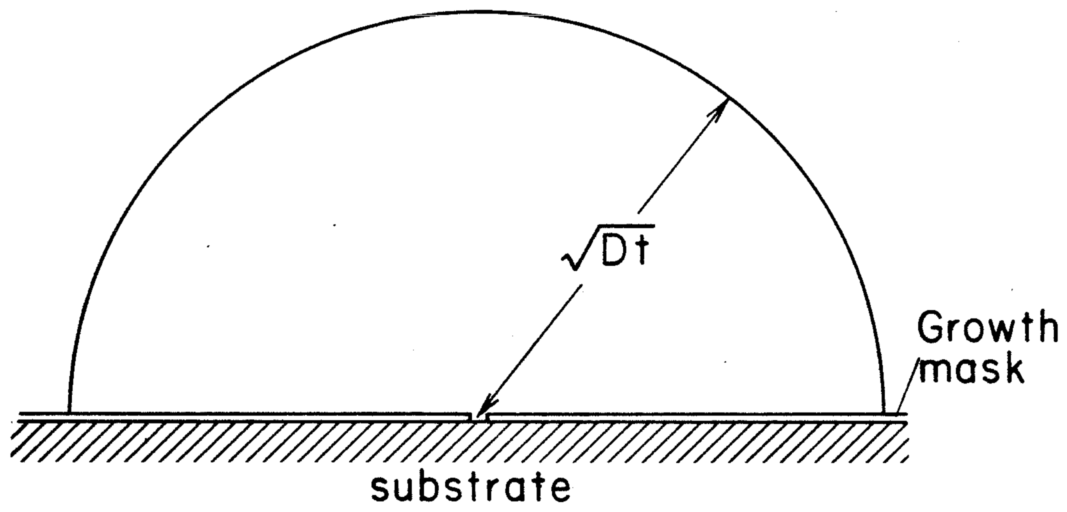

Fig. 3.5 Growth on a very narrow stripe. Growth rate is proportional to area of semicircle

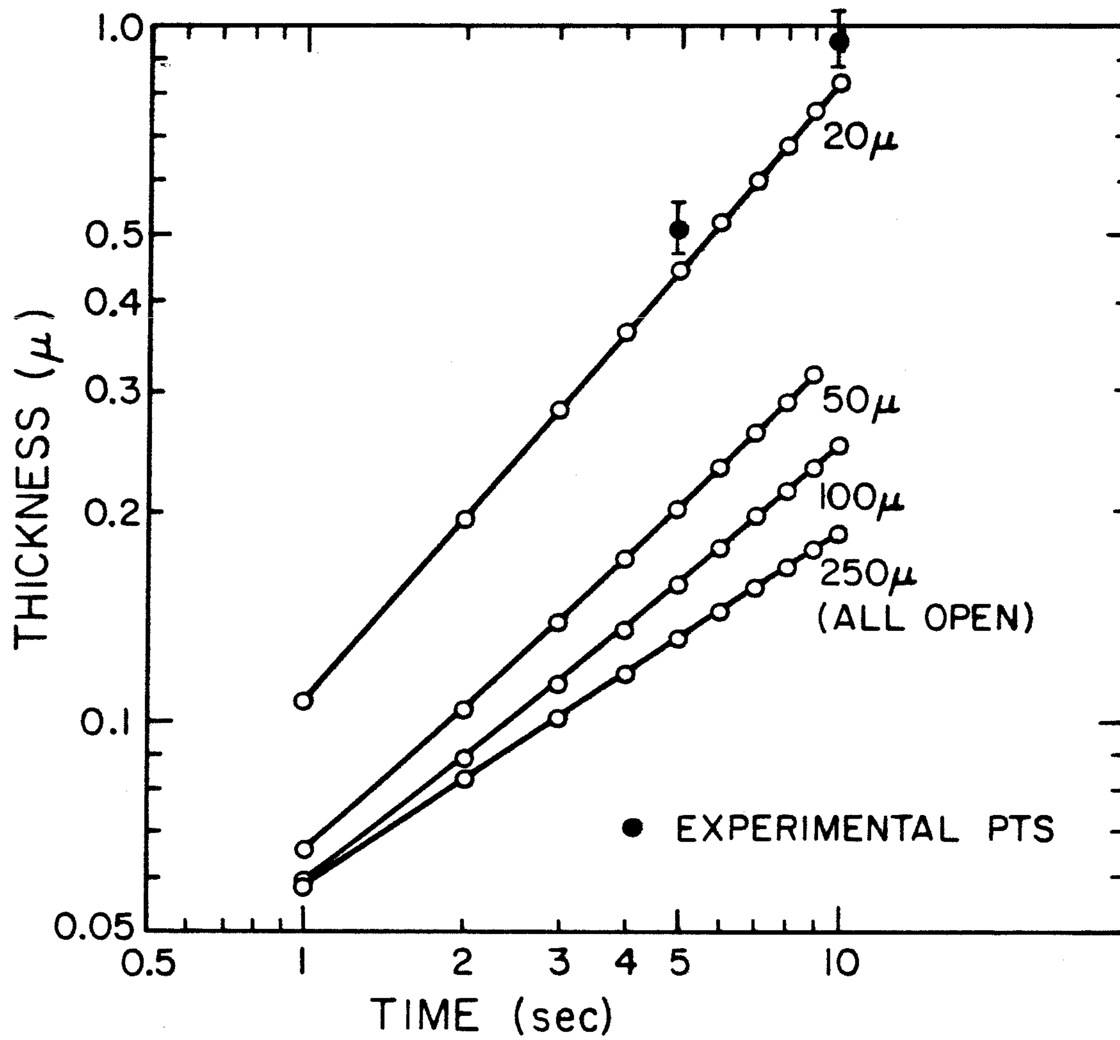

Fig. 3.6 Calculated growth thickness vs time of LPE InP at 650°C for different stripe widths.

Limitation due to the uncontrollable growth rates can be overcome by opening up "dummy" areas adjacent to the stripes. The boundary conditions for this case are modified such that

$$D\frac{\partial C}{\partial z}(z=0) = \frac{\partial P}{\partial t} \qquad \text{opened areas} \qquad (3.7a)$$

$$C(x,0,t) = C_1 \qquad \text{opened areas} \qquad (3.7b)$$

$$D\frac{\partial C}{\partial z}(z=0) = 0 \qquad \text{masked areas} \qquad (3.7c)$$

This is illustrated in Fig. 3.7, where the calculations show that the growth rate inside the stripe is only slightly higher than that in a completely unmasked area. This improved technique allows well-controlled liquid phase epitaxial growth over the desired areas.

3.3 Low Threshold Embedded Lasers

The above ideas were applied in practice and resulted in very controllable growths that made possible the reproducible fabrication of lasers with low thresholds. These lasers were grown by the two-phase method [9,10]. The substrate was prepared by first cleaning in organic solvents, then rinsed in de-ionized water. Thereafter it was placed in concentrated nitric acid for three to five minutes, rinsed in de-ionized water and then etched in 1% bromine methanol for two minutes. This ensures a clean substrate surface. A thin layer (~ 1000Å) of silicon nitride was deposited at ~ 700 °C. Even though the deposition temperature was high, little thermal damage of the substrate occurred because of the short time involved (~ 20sec). Except for two narrow adjacent stripes, the remaining silicon nitride were removed by conventional photolithography and chemical etching. The masked substrate was again cleaned and etched with dilute bromine methanol before loading into the boat. After flushing with palladium-purified

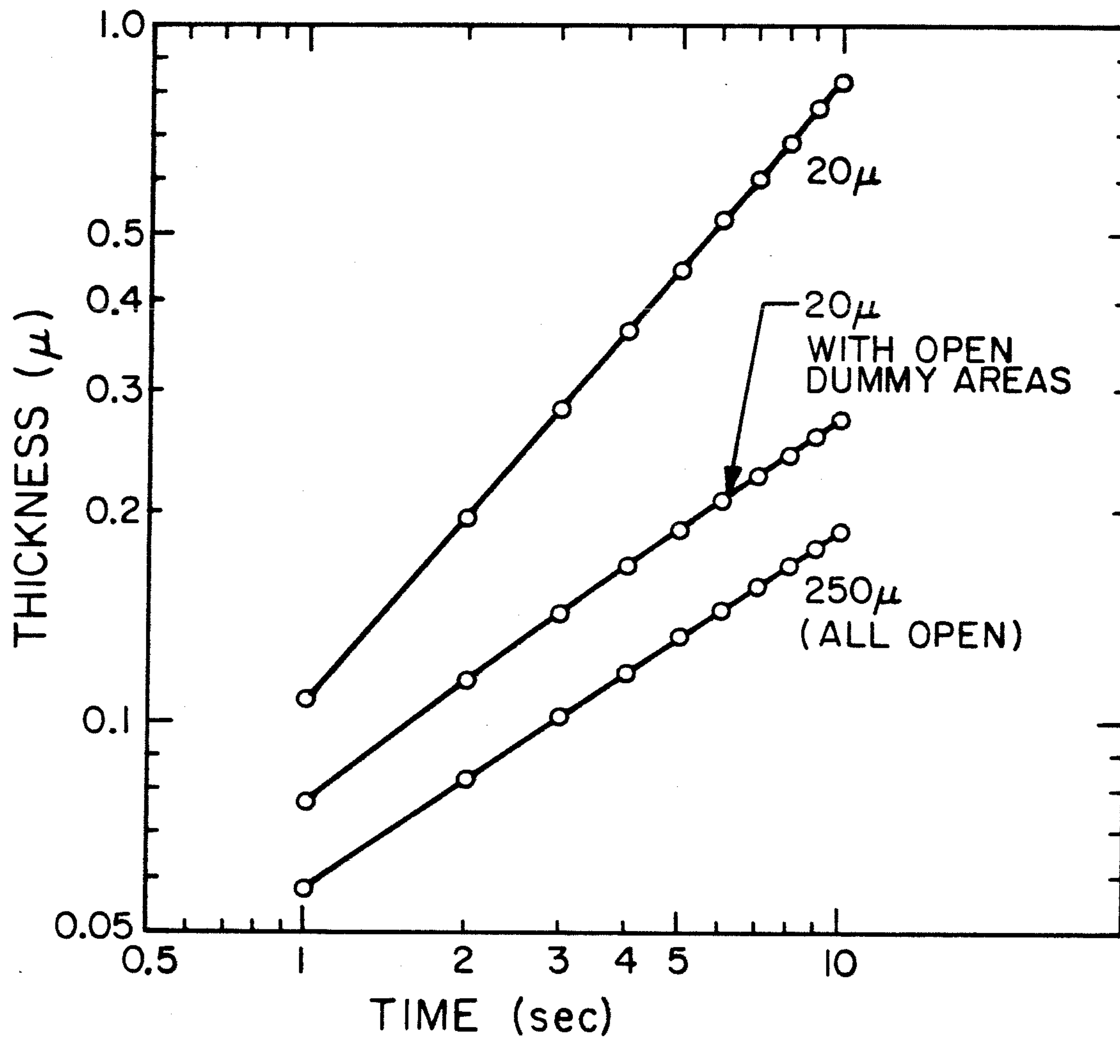

Fig. 3.7 Calculated growth thickness vs time of LPE InP at 650°C for a 20 μm stripe with and without openning of dummy areas.

hydrogen, the furnace was heated to 675 °C for one hour and then cooled at 0.7 °C/min. During this time the substrate was prevented from thermal damage by covering it with an InP wafer which supplied a phosphorus overpressure. Then, three layers, InP (n ~ $5\times10^{17}cm^{-3}$), GaInAsP (undoped) and InP (p ~ $2\times10^{18}cm^{-3}$) were consecutively grown. The quaternary active region was grown at 635 °C. The growth of the first layer was quite critical. It had to reach above the level of the mask in order for the GaInAsP active layer to be completely embedded in InP, otherwise, a mesa type structure would result. A cross section of a good growth on [011] channels is shown in Fig. 3.8. Interestingly, growth on $[01\bar{1}]$ channels (Fig. 3.9) did not produce embedded quaternary layers. Apparently, for narrow stripes, facet formation was unavoidable, and deposition of new material seemed to prefer some facets to others.

After growth, a layer of CVD silicon dioxide was deposited over the entire wafer and contact stripes were opened by photolithography. In this step, it was important to make the openings only on the top of the ridge or the junctions could be shorted. This requirement was met in practice without undue difficulty since the spun-on photoresist was thinner on top of the ridge and thicker in the two adjacent valleys. Au-Zn contacts were evaporated and alloyed at 420 °C. The wafer was lapped down to 75 μm on the substrate side and Au-Ge was evaporated to form the n-contact. Alloying of the n-contact was performed at 250 °C. Bars of 200-300 μm long lasers were cleaved and tested with 100 nsec current pulses.

For a laser shown in Fig. 3.8, with a 0.2 μm thick and 4 μm wide active layer, the pulsed threshold varied between 50 and 70 mA. The lowest achieved was 45 mA. A typical L-I characteristic is shown in Fig. 3.10. The external differential quantum efficiency including both facets was ~ 40%. A spectrum of such a laser is shown in Fig. 3.11.

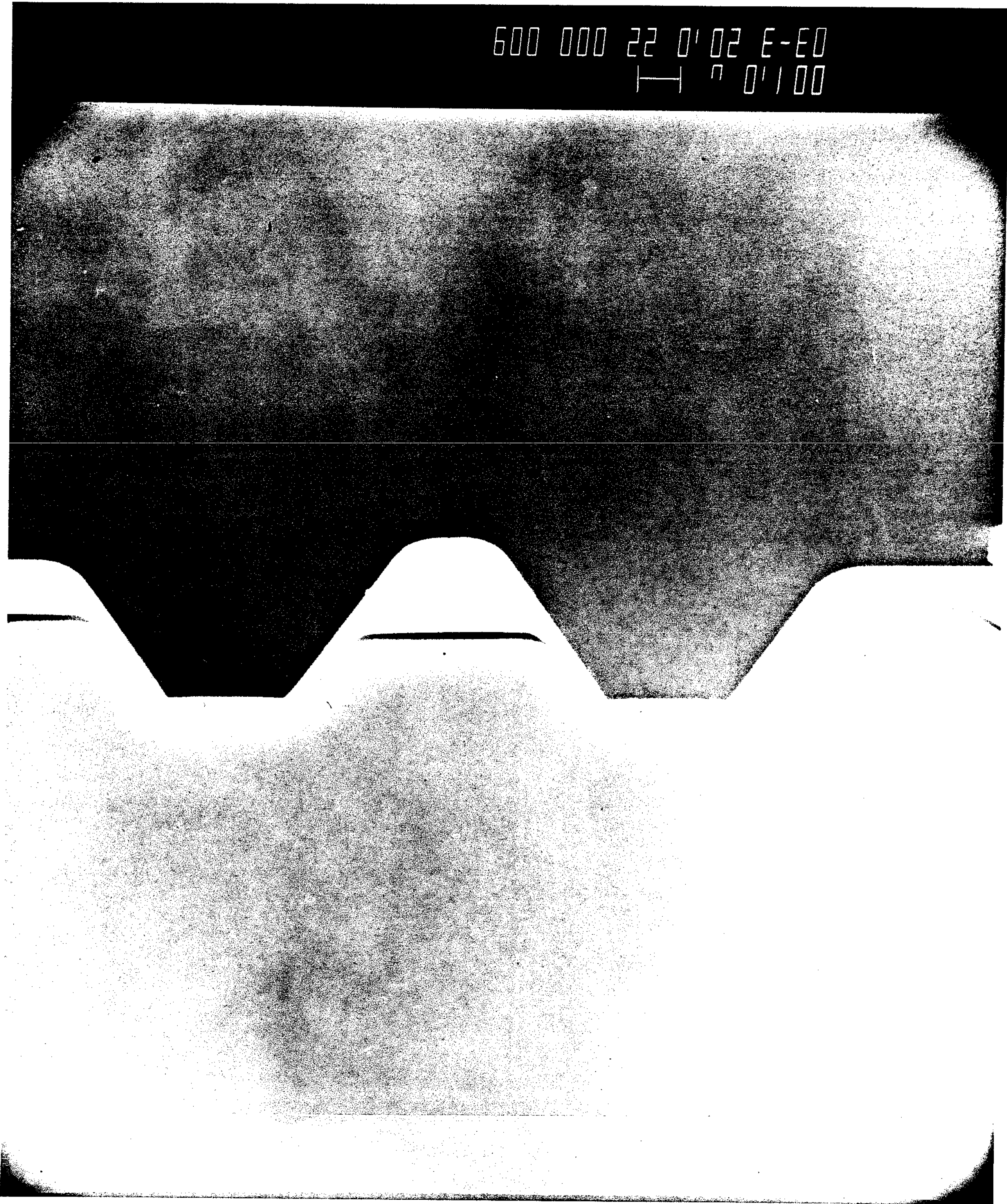

Fig. 3.8 Embedded Heterostructure grown on 7 μm stripe along [011] channels.

Fig. 3.9 3-layer structure grown on 7 μm stripe along $[01\bar{1}]$ channels.

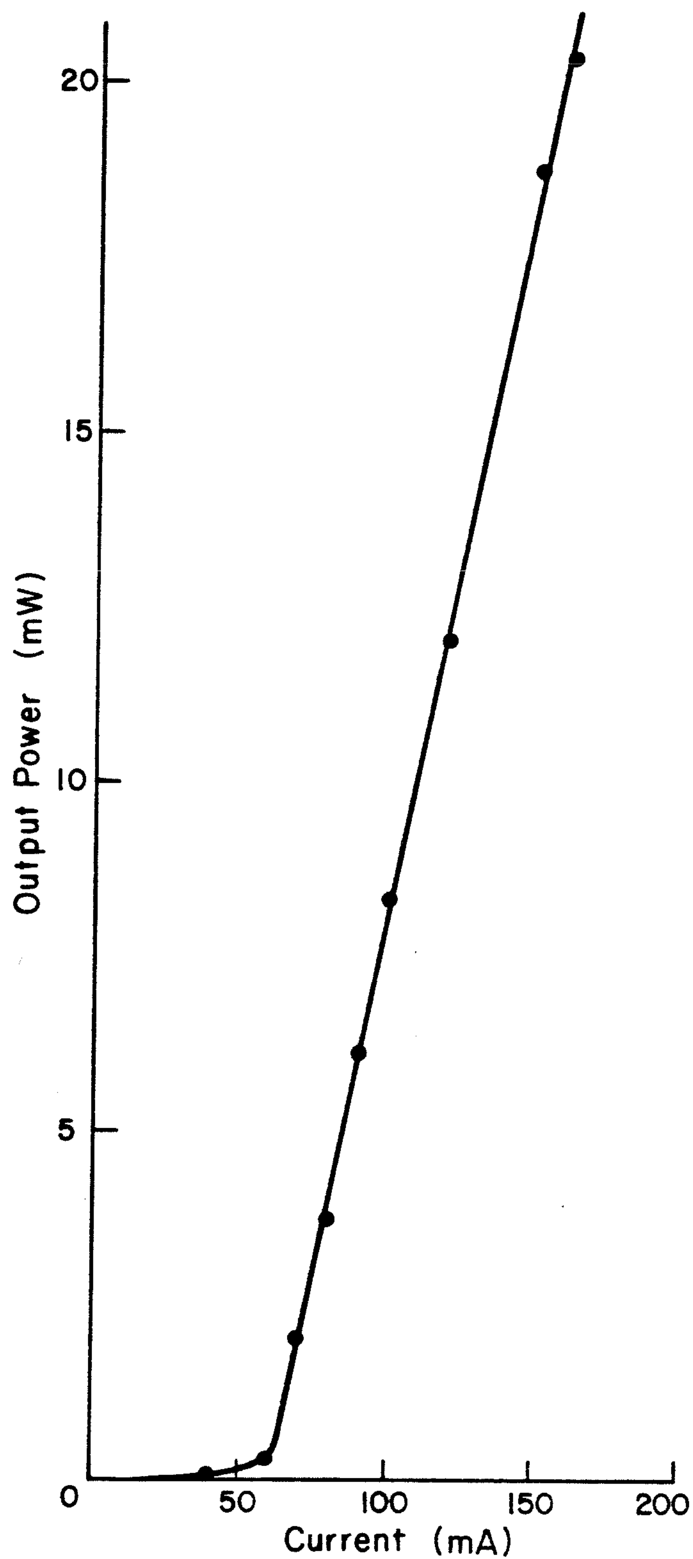

Fig. 3.10 L-I characteristic of an Embedded Laser.

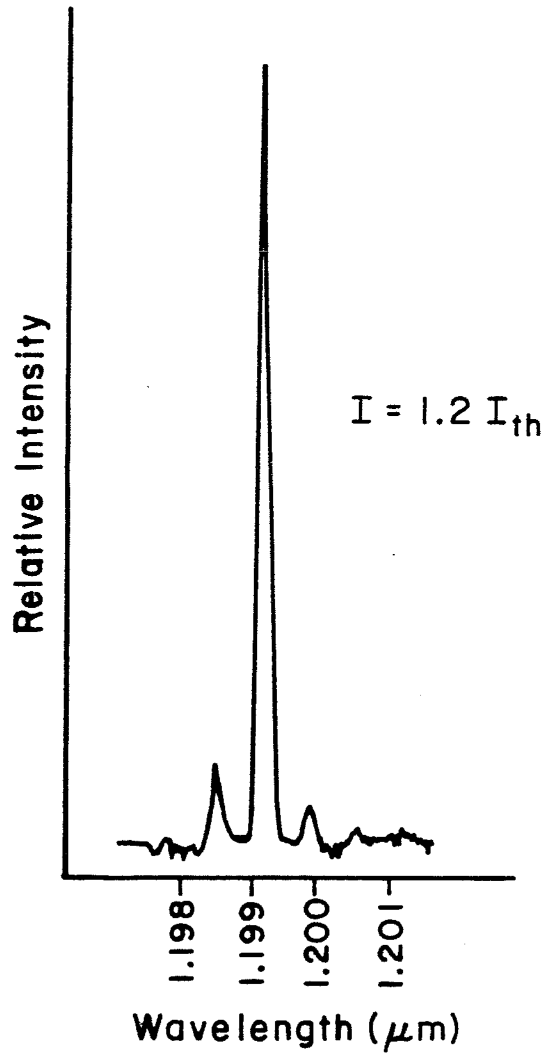

Fig. 3.11 Spectrum of an Embedded Laser.

To compare the threshold current of this laser with that of an oxide stripe laser, a structure with a 0.7 μm thick active layer was also grown. On layers grown on the "dummy" areas, 7 μm stripes were opened in the silicon dioxide, in addition to the openings on top of the embedded laser ridge. Thus a cleaved rectangular strip of wafer contained both types of lasers. The results were shown in Fig. 3.12. The oxide stripe laser possessed higher threshold current and lower differential quantum efficiency due to current spreading that plagues this structure. This confirmed the excellent current and carrier confinement attained in the embedded laser.

In our experience, the growth of layers on top of the ridge ceased whenever a triangular cross section was reached. Since the top cladding layer should at least be about 1 μm thick to prevent barrier leakage of carriers, this may place a limit on the size of the active region, and hence, a lower limit on the threshold current. Nevertheless, through increasing the cooling rate or the degree of supersaturation in the solution, more material could be deposited even after the triangular cross section had been reached (Fig. 3.13). With perfection of this technique, lasers with even lower thresholds could be fabricated.

A measurement of threshold current vs temperature of the embedded laser has also been conducted. The results are summarized in Fig. 3.14. The values can be said to vary ~ $\exp(T/T_o)$ where T_o=65°K. This large dependence near room temperature is also typical of all other GaInAsP/InP lasers fabricated by other researchers [11,12,13]. An investigation into the origin of this phenomenon has led to the work described in the next chapter.

In conclusion, we have developed the technology of embedded epitaxial growth of laser structures that possess low threshold currents. Our result of 45 mA for a 4 μm wide active region is comparable to that for a state of art buried heterostructure laser. One clear advantage of our structure is its simplicity and

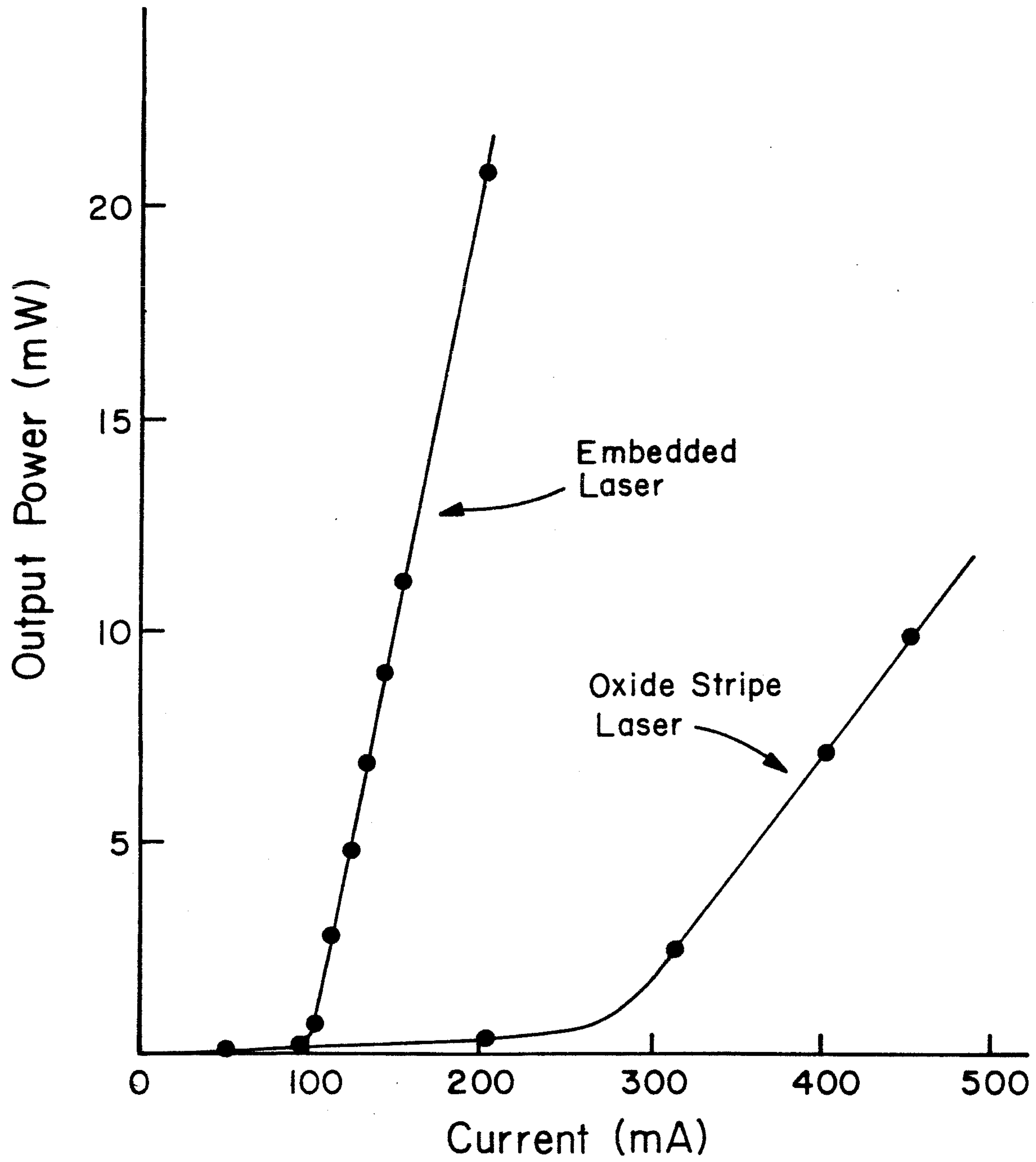

Fig. 3.12 L-I characteristics of Embedded Laser and Oxide-Stripe Lasers procesed from the same wafer.

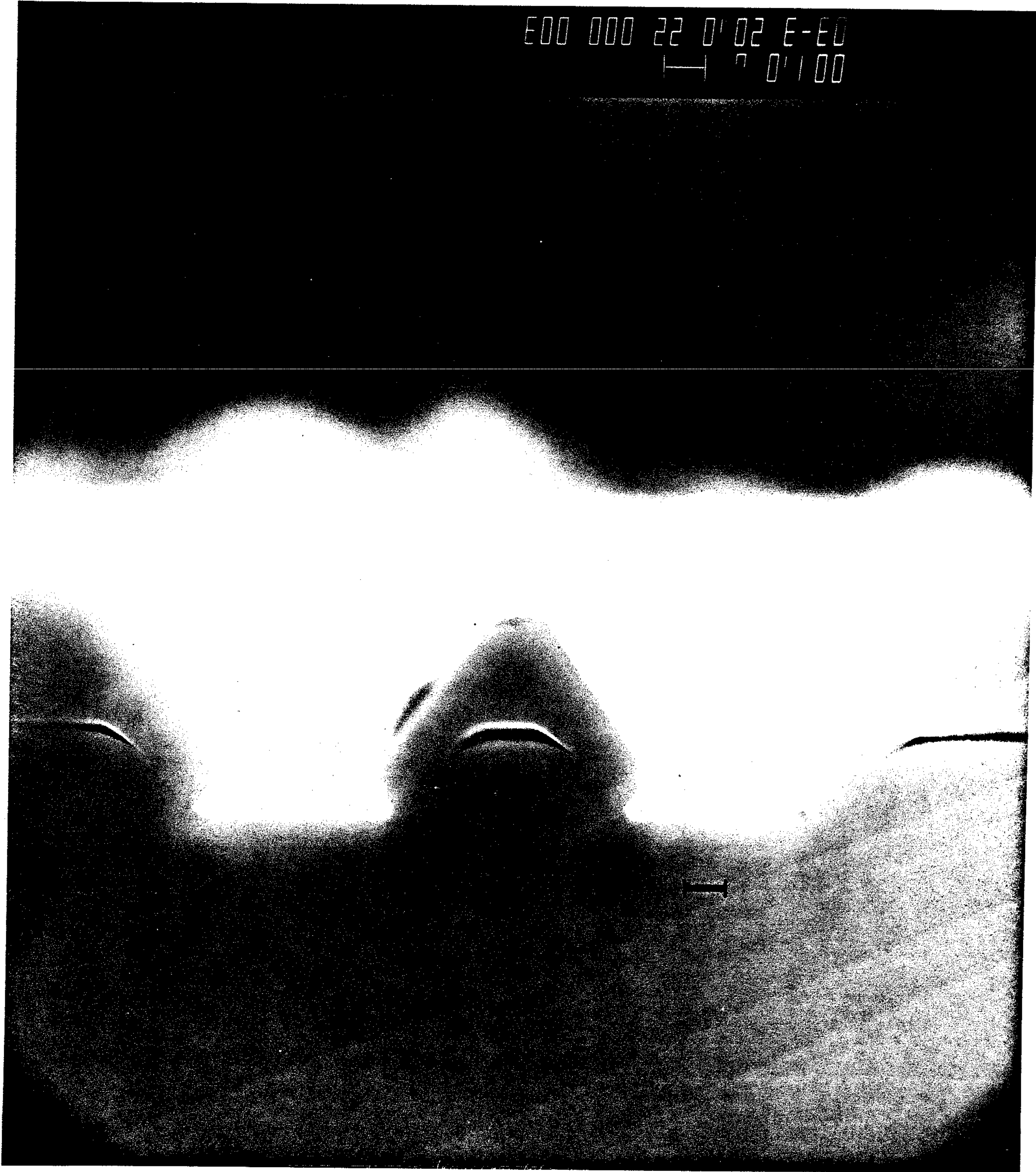

Fig. 3.13 Overgrowth of layer with improved technique.

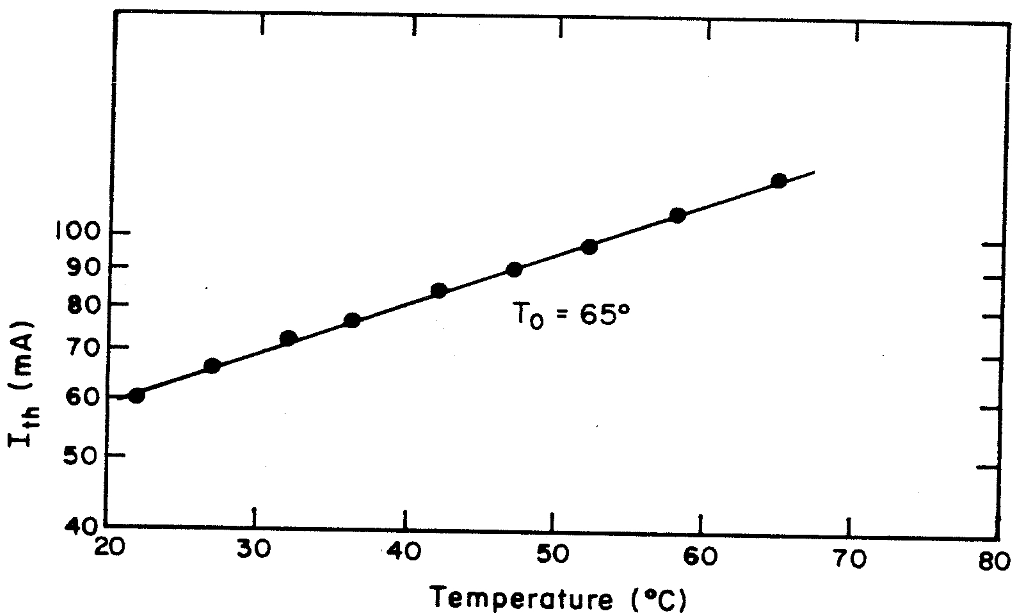

Fig. 3.14 Threshold current vs temperature plot for an Embedded Laser.

ease of fabrication. Problems associated with regrowth steps and accurate photolithographic alignment are absent. This novel technique should find applications in future epitaxial growth of new optoelectronic devices.

References - Chapter 3

1. see for example, H. C. Casey, Jr. and M. B. Panish, **Heterostructure Lasers: Part A, Fundamental Principles** , Academic Press, New York (1978)

2. T.Tsukada, "GaAs-$Ga_{1-x}Al_xAs$ Buried-Heterostructure Injection Lasers," J. Appl. Phys. **45** , 4899(1974)

3. M. Hirao, A. doi, S. Tsuji, M. Nakamura, and K. Aiki, "Fabrication and Characterization of Narrow Stripe InGaAsP/InP Buried Heterostructure Lasers," J. Appl. Phys. **51** , 4539(1980)

4. I. Samid, C. P. Lee, A. Gover, and A. Yariv, "Embedded Heterostructure Epitaxy: A Technique for Two-Dimensional Thin-Film Definitions," Appl. Phys. Lett. **27** , 405(1975)

5. C. P. Lee, I. Samid, A. Gover, and A. Yariv, "Low-Threshold Room-Temperature Embedded Heterostructure Lasers," Appl. Phys. Lett. **29** , 365(1976)

6. J. Katz, S. Margalit, D. Wilt, P. C. Chen, and A. Yariv, "Single-Growth Embedded Epitaxy AlGaAs Injection Lasers with Extremely Low Threshold Currents," Appl. Phys. Lett. **37** , 987(1980)

7. J. J. Hsieh, "Thickness and Surface Morphology of GaAs LPE Layers Grown by Supercooling, Step-Cooling, Equilibrium, and Two-Phase Solution Techniques," J. Cryst. Gr. **27** , 49(1974)

8. J. J. Hsieh, "Thickness of InP Layers Grown by LPE from Supercooled Solutions," **GaAs**and , Inst. Phys. Conf. No. 33b, 74(1977)

9. S. Araio Y. Suetmatsu, and Y. Itaya, "1.11-1.67 μm (100) GaInAsP/InP Injection Lasers Prepared by Liquid Phase Epitaxy," IEEE J. Quant. Electron. **QE-16** , 197(1980)

10. M. A. Pollack, R. E. Nahory, J. C. DeWinter, and A. A. Ballman, "Liquid-Phase

Epitaxial $In_{1-x}Ga_xAs_yP_{1-y}$ Lattice-Matched to < 100> InP over the Complete Wavelength $0.92 \leq \lambda \leq 1.65 \mu m$," Appl. Phys. Lett. **33** , 314(1978)

11. Y. Horikoshi and Y. Furukawa, 'Temperature Sensitive Threshold Current of InGaAsP-InP Double Heterostructure Lasers," Japan. J. Appl. Phys. **18** , 809(1979)

12. M. Yano, H. Nishi, and M. Takasagawa, 'Temperature Characteristics of Threshold Current in InGaAsP/InP Double Heterostructure Lasers," J. Appl. Phys. **51** , 4022(1980)

13. R. E. Nahory, M. A. Pollack, and J. C. DeWinter, 'Temperature Dependence of InGaAsP Double-Heterostructure Laser Characteristics," Electron. Lett. **15** , 695(1979)

Chapter 4
Interband Auger Recombination in GaInAsP/InP Semiconductor Lasers

4.1 Introduction

For many applications, semiconductor lasers must operate under adverse conditions. In some cases, changes in the environment may affect their performances. While many factors such as humidity can be simply eliminated, the effects of temperature changes cannot be removed without resort to fairly cumbersome electronic circuitry. In general, all semiconductor lasers exhibit threshold currents that increase with temperature. The rate of increase varies with material system and from structure to structure. For most lasers, it is found empirically that I_{th} changes with temperature T as $I \sim \exp(T/T_o)$. A typical plot of $\log(I_{th})$ vs T for both GaAlAs/GaAs and GaInAsP/InP lasers is shown in Fig. 4.1.

As indicated by the plot, semiconductor injection lasers using the quaternary compound InGaAsP as active layers generally exhibit threshold current densities that depend strongly on temperature. They are characterized by a T_o of about 110 °K at low temperatures and a low T_o ranging from 50–80 °K for temperatures above about 220 °K [1-3]. This value is considerably lower than that of GaAlAs/GaAs lasers, which is typically greater than 110 °K. Low values of T_o pose a serious limitation on the performance of semiconductor lasers at elevated temperatures, and also limit the maximum temerature for which cw operation can be maintained. It is therefore important to understand the origin and nature of this phenomenon in the quaternary GaInAsP/InP lasers.

While the behavior of the GaInAsP/InP lasers at low temperatures is attributed to the same mechanism responsible in GaAlAs/GaAs lasers, the lower T_o at

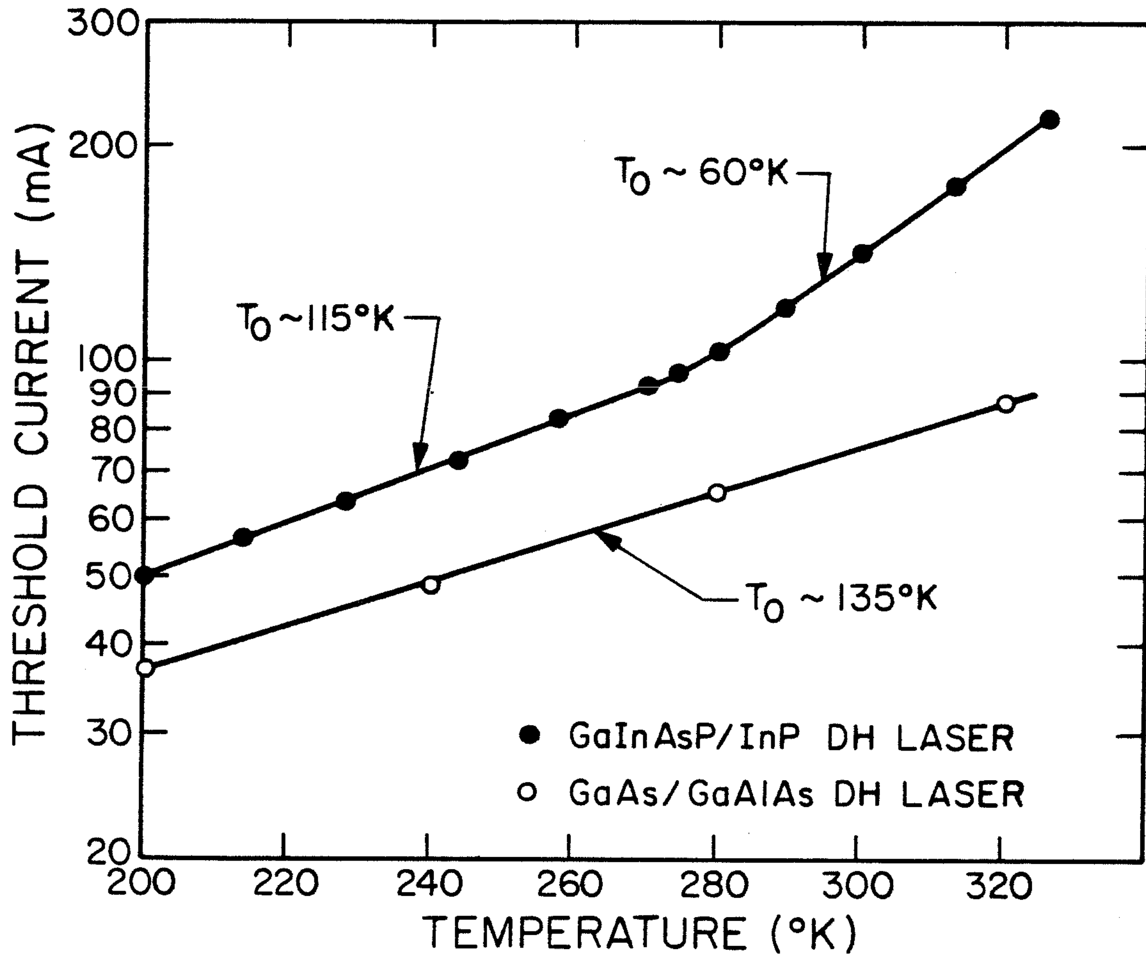

Fig. 4.1 Temperature characteristics of threshold currents of GaAlAs/GaAs and InGaAsP/InP lasers.

higher temperatures indicate another mechanism is dominant. For GaInAsP lasers, the onset of the rapid increase in threshold current with temperature at about 220–250 °K is accompanied by a sharp decrease in the carrier lifetime and the spontaneous recombination efficiency [1,3,4,5]. In this chapter, we present calculations on the interband Auger recombination lifetimes of two Auger processes in order to correlate measured threshold current densities and carrier lifetimes for GaInAsP and GaInAsSb lasers. Good agreement with experimental data is obtained for lasers with low nominal threshold current densities. These results demonstrate the importance of Auger recombination in the threshold characteristics of GaInAsP/InP lasers. Various mechanisms have been proposed to account for the reduction in carrier lifetime and low T_o [1,6,7]. These are discussed in the next section.

4.2 VARIOUS MECHANISMS THAT AFFECT TEMPERATURE THRESHOLD CHARACTERISTICS

Many factors influence the temperature characteristics of threshold in semiconductor lasers. The major ones that are considered for GaInAsP/InP lasers are:

a) carrier leakage over the heterobarrier.

In double heterostructure lasers, leakage currents are, aside from structural defects, determined mainly by carrier diffusion. The dominant process has been shown in the GaAlAs/GaAs case to be normal (Γ) electron leakage [8], illustrated in Fig. 4.2. Electrons are excited thermally from the active region to the normal conduction band of the p-cladding region and diffuse away. The resulting current is given by

$$j_\Gamma = \frac{D_\Gamma}{L_\Gamma} e n_\Gamma \tag{4.1}$$

where D_Γ is the electron diffusion coefficient, L_Γ is the effective electron diffusion

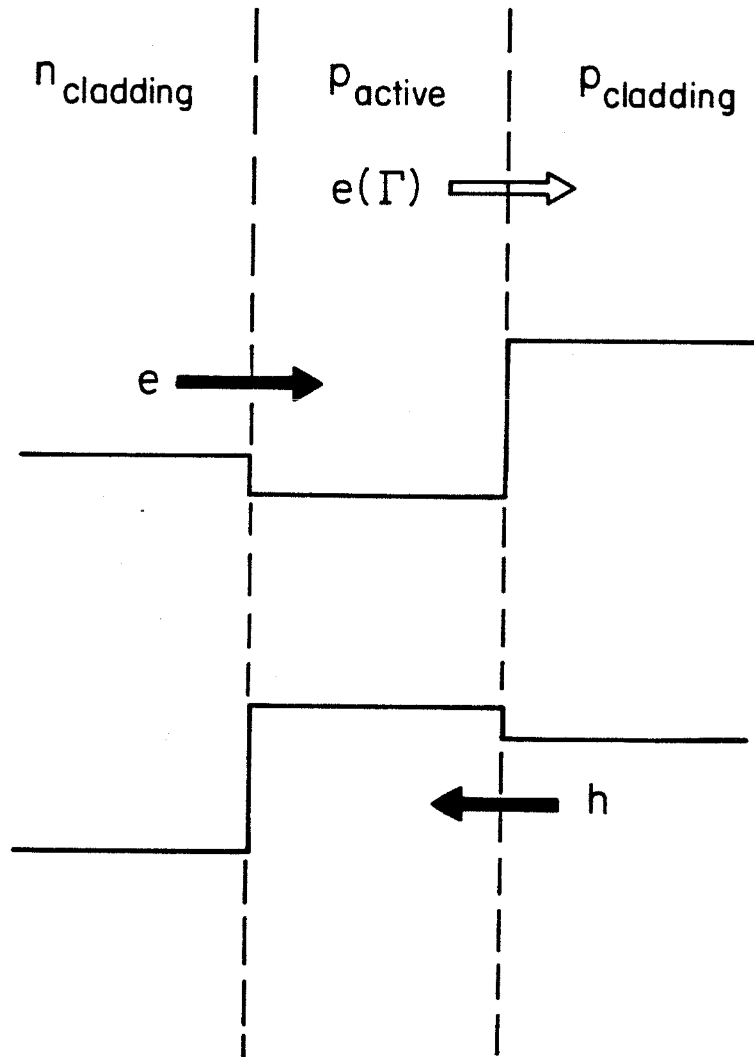

Fig. 4.2 Schematic of leakage currents in a DH structure.

length, and n_Γ, the density of excited carriers in the conduction band of the p cladding layer at the heterointerface with the active region, is given by

$$n_\Gamma = N_c(T)[\frac{(p_{act}+n_1)}{p_{clad}}]\exp[\frac{(E_1-\Delta E)}{kT}]\,, \qquad (4.2)$$

where n_1 and E_1 are the injected electron density and associated Fermi energy in the active region measured from the bottom of the conduction band. ΔE is the heterojunction step energy, and $N_c(T)$ the effective density of states in the conduction band of the active layer. It has been shown in the GaAlAs/GaAs system that lasers with small barrier heights (<0.3 eV) possess a much lower T_o than those with larger barrier steps. The small step is insufficient in preventing the injected carriers from escaping the active region by hopping over the barrier. In the case of GaInAsP/InP lasers, carrier leakage may account for the low T_o of lasers with small heterobarrier steps, but for lasers at wavelengths longer than 1.1 μm, the step should already be large enough to prevent any significant leakage. Furthermore, the InP luminescence intensity peak in the cladding layers expected from the leakage current is not experimentally observed [1]. Therefore this mechanism cannot be responsible for the observed low T_o in the GaInAsP/InP lasers.

b) Non-radiative traps

When deep-level defects or interfacial states become thermally activated, they act as centers through which non-radiative recombination can occur. The non-radiative lifetime τ_{NR} can be written as

$$\tau_{NR} \propto \exp(\frac{E_a}{kT}) \qquad (4.3)$$

where E_a is the activation energy. Some authors have reported that an activation energy between 0.1 eV to 0.3 eV is required to fit the observed data near

room temperature [1,4,9]. Attempts at identifying these "traps" through Deep Level Transient Spectroscopy (DLTS) produced ambiguous results. Other methods have also been fruitless. Moreover, measurements of devices operating in the LED mode demonstrated that the carrier recombination rate varies roughly as n^a, where $2< a< 4$, while the expected rate for these traps has $1< a< 2$.

c) Non-radiative Auger Recombination

It is well known that the Auger process can become dominant in low bandgap materials at high temperatures. Thus some authors have pointed out that these non-radiative processes may be responsible for the observed phenomena [5,10]. However, most discussions thus far have been inadequate, as will be mentioned later.

Fig. 4.3 shows two normal Auger recombination processes that should be significant at high temperatures for small bandgap semiconductors [11,12]. In the CHCC process, an electron in the conduction band recombines with a hole in the valence band. The energy and momentum are imparted to another electron in the conduction band for conservation. The CHSH process is similar, except that the energy and momentum are taken up by an electron that makes a transition from the split-off hole band into the valence band.

It is clear that the probability for such transitions increases with carrier concentration. Also, the criterion that both energy and momentum be conserved simultaneously places stringent restrictions on the participating particles, with the result that these transitions occur more easily at higher temperatures. Therefore, this may account for the sharp decrease in carrier lifetime.

4.3 The CHCC and CHSH Auger Processes

The formalism used here is similar to previous works on the CHCC process in ref. 5 and the CHSH process in ref. 13. However, we differ in some important

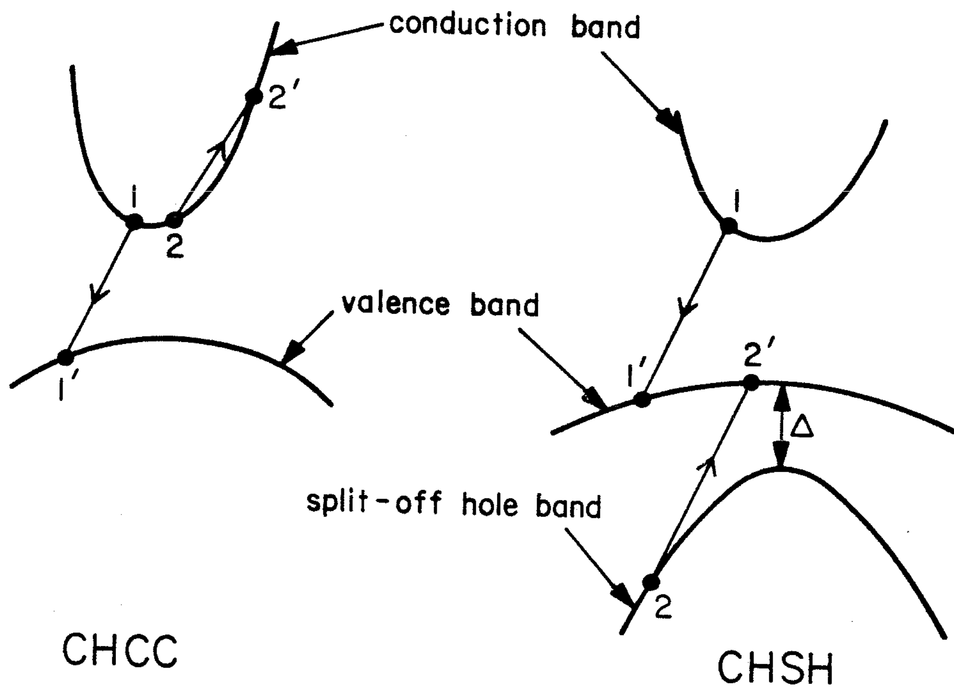

Fig. 4.3 Schematic of the normal CHCC and the CHSH Auger processess.

basic assumptions. In addition, we have applied experimental data into the calculation rather than to rely solely on theoretical numbers.

The first assumption we make is that carrier densities in the active region can be described by quasi-fermi levels. This assumption is usually valid in semiconductor lasers. Secondly, parabolic band expressions are assumed and no bandtailing is accounted for. To first order, this should not affect our results because carriers at the band minimum have little probability of participating in an Auger process due to the requirement of simultaneous energy and momentum conservation. Furthermore, we assume that injection level is high at threshold, i.e., $n_{th} >>$ background doping, and n=p to maintain charge neutrality.

As opposed to ref. 5, where the calculations were carried out under the assumption that both the conduction and the valence bands are non-degenerate, and that the injection level is low, we have accounted for degeneracy of the conduction band at lasing. Degeneracy in at least one band is necessary for lasing. However, at typical injection levels of a laser, the valence band remains non-degenerate.

The carrier concentration needed for lasing can be obtained by balancing cavity and absorption losses with gain as calculated from Stern's matrix element. Nevertheless, we elected to obtain n_{th} from experimental measurements of the threshold current density, J_{th}, and carrier lifetime, τ, as functions of temperature, by applying the relation

$$\frac{J_{th}}{ed} = \frac{n_{th}}{\tau} \tag{4.4}$$

where e is the electronic charge, and d is the active layer thickness. This procedure would yield accurate values of n_{th} for high quality lasers with low nominal threshold current density J_{th}/d, which shows the absence of other current

loss mechanisms.

The expression for the band to band Auger recombination is derived from perturbation theory by using a screened Coulomb interaction Hamiltonian. The transition probability per unit time due to a perturbation starting instantaneously at time $t = 0$ is given by Fermi's golden rule

$$P = \frac{2\pi}{\hbar} |H'_{if}|^2 \rho(E). \tag{4.5}$$

Here, H'_{if} is the transition matrix element of the perturbation operator H' and $\rho(E)$ is the joint density of states including population factors. For the interaction between two electrons separated by distance r in a semiconductor with permittivity ε, the perturbation operator is

$$H' = \frac{e^2}{4\pi\varepsilon r} \exp(-\frac{r}{L_D}) , \tag{4.6}$$

where L_D is the Debye length. The umklapp processes have been shown to be negligible in this case, and the transition rate can then be written, after Huldt, as [11],

$$P=\frac{2\pi}{\hbar}(2\beta)2(\frac{V}{(2\pi)^3})^3(\frac{e^2}{\varepsilon V})^2 \int\int\int \frac{|F_1F_2|^2}{(\,|\vec{k}_1-\vec{k}_{1'}|^2 + L_D^{-2}\,)^2}$$

$$\times\ [f_1f_2(1-f_{1'})(1-f_{2'})-(1-f_1)(1-f_2)f_{1'}f_{2'}]\delta(E_f-E_i)d\vec{k}_1 d\vec{k}_{1'} d\vec{k}_{2'} \tag{4.7}$$

In the above, the f's are the Fermi factors, $E_{f,i}$ are the final and initial energies of the particles respectively, L_D is the usual screening length, and $2 < 2\beta < 3$ due to spin symmetry. The Fermi factor is given by

$$f_j = \frac{1}{1+\exp(\frac{F_j-E_j}{kT})} \tag{4.8}$$

where F_j and E_j are the quasi-fermi and bandedge energies of particle j. The Fermi energy for the conduction band is obtained from carrier concentration n by

$$\frac{F_j-E_j}{kT} = \ln\left(\frac{n}{N_c}\right)+2^{-3/2}\left(\frac{n}{N_c}\right) \tag{4.9}$$

N_c is the effective density of states in the conduction band. This expression gives very accurate values of the fermi energy for carrier densities near lasing.

In contrast, the valence band is typically non-degenerate and Boltzman statistics are used.

$$p = N_v \exp\left(\frac{F_v-E_v}{kT}\right) \tag{4.10}$$

In principle, determination of the overlap integrals F_1 and F_2 requires knowledge of the electronic wave functions u_c. The approach of Antoncik and Landsberg [12] based on the $\vec{k}\cdot\vec{p}$ method is adopted which allows interband overlap integrals to be approximately calculated using first-order perturbation theory, for small differences $|\vec{k}_1-\vec{k}_1'|$. This has the advantage that exact knowledge of the wave functions are not required. The overlap integrals $|F_1F_2|^2$ are then given by

$$|F_1F_2|^2 \doteq \frac{\hbar^2}{2m_eE_g} f_{CV} |\vec{k}_1-\vec{k}_1'|^2 \tag{4.11}$$

for the CHCC process [13] and

$$|F_1F_2|^2 \doteq \alpha_{CH}\alpha_{SH}\frac{|\vec{k}_1-\vec{k}_1'|^2}{E_g^2} \tag{4.12}$$

for the CHSH process [14,15]. In the above equations, m_e is the electron mass, E_g is the bandgap energy, and f_{CV} is the oscillator strength. The α_{CH} and α_{SH} are the

Symbol	$In_{1-x}Ga_xAs_yP_{1-y}$
ε	$x\varepsilon_{GaAs} + (y-x)\varepsilon_{InAs} + (1-y)\varepsilon_{InP}$
m_c	$(.08-.039)y$
m_v	$(1-y)(.79x + .45(1-x)) + y(.45x + .4(1-x))$
m_s	$.17x + .083(y-x) + .15(1-y)$
Δ	$.11 + .421y - .152y^2$

Table 4.1 Parameters used in calculation of Auger lifetimes.

overlap parameters as given in ref. 14. The effective masses for electron and hole, and the spin-orbit coupling Δ are taken from refs. 16 and 17 respectively. Table 4.1 sumarizes the parameters used in our calculations. The three-fold integrations were calculated numerically assuming parabolic bands, and the Auger lifetime is obtained from the expression

$$\tau_A = \frac{\Delta n}{P} \tag{4.13}$$

where Δn is the injected carrier density at threshold. In the calculation, the Fermi levels are calculated from experimental values of n_{th}, whence degeneracy is fully accounted for in the conduction band. It is also assumed that injection level is high, so that $\Delta n \doteq n_{th}$, an assumption which is good for injection lasers.

4.4 Comparison of Calculated and Measured Lifetimes

Data for lasers emitting at 1.1, 1.27, 1.3 and 1.48 μm were taken respectively from references 1, 3, 5 and 4. To account for current spreading under the stripes, the measured J_{th} was divided by factors of 1.6 and 1.2 as appropriate for 15 and 20 μm stripes to obtain the actual current density in the active region [18].

For comparison, the calculated and experimental carrier lifetime at 300 °K are listed in table 4.2, along with other characteristics of the lasers. The total carrier lifetime is obtained from the sum of the radiative and Auger effects, by $\frac{1}{\tau} = \frac{1}{\tau_{rad}} + \frac{1}{\tau_{CHCC}} + \frac{1}{\tau_{CHSH}}$. The radiative lifetime is obtained by extrapolation of experimental values at low temperatures. As is evident from Table 4.2 and Figs. 4.4-4.7, reasonable agreement was obtained for lasers with low nominal threshold current density. When the nominal threshold current density is high, the calculated Auger lifetimes are significantly shorter than the observed values. This is due to the high apparent carrier concentration resulting from the high threshold current density, which implies the existence of additional current loss

Wavelength (μm)	J_{th}/d (kA/cm$^2\mu$m)	τ_{exp} (ns)	τ_{cal} (ns)
1.1	-	4.0	4.2
1.27	14.0	2.0	1.4
1.3	9.0	2.3	2.0
1.48	7.6	1.7	2.0

Comparison of measured and calculated carrier lifetimes for GaInAsP lasers at 300 °K. Better agreement is obtained for lasers with low J_{th}/d.

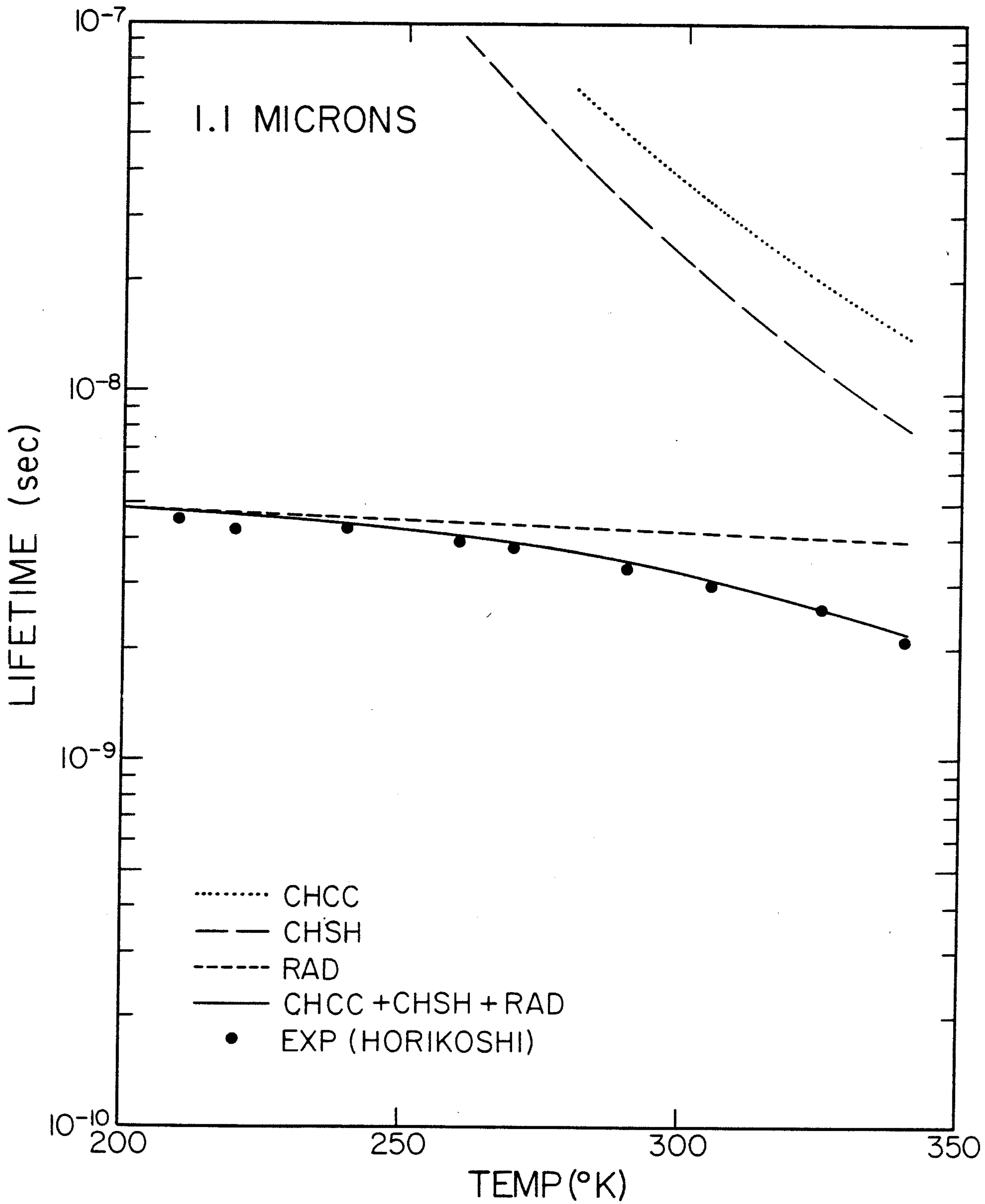

Fig. 4.4 Experimental and calculated carrier lifetimes for a 1.1 μm InGaAsP/InP laser.

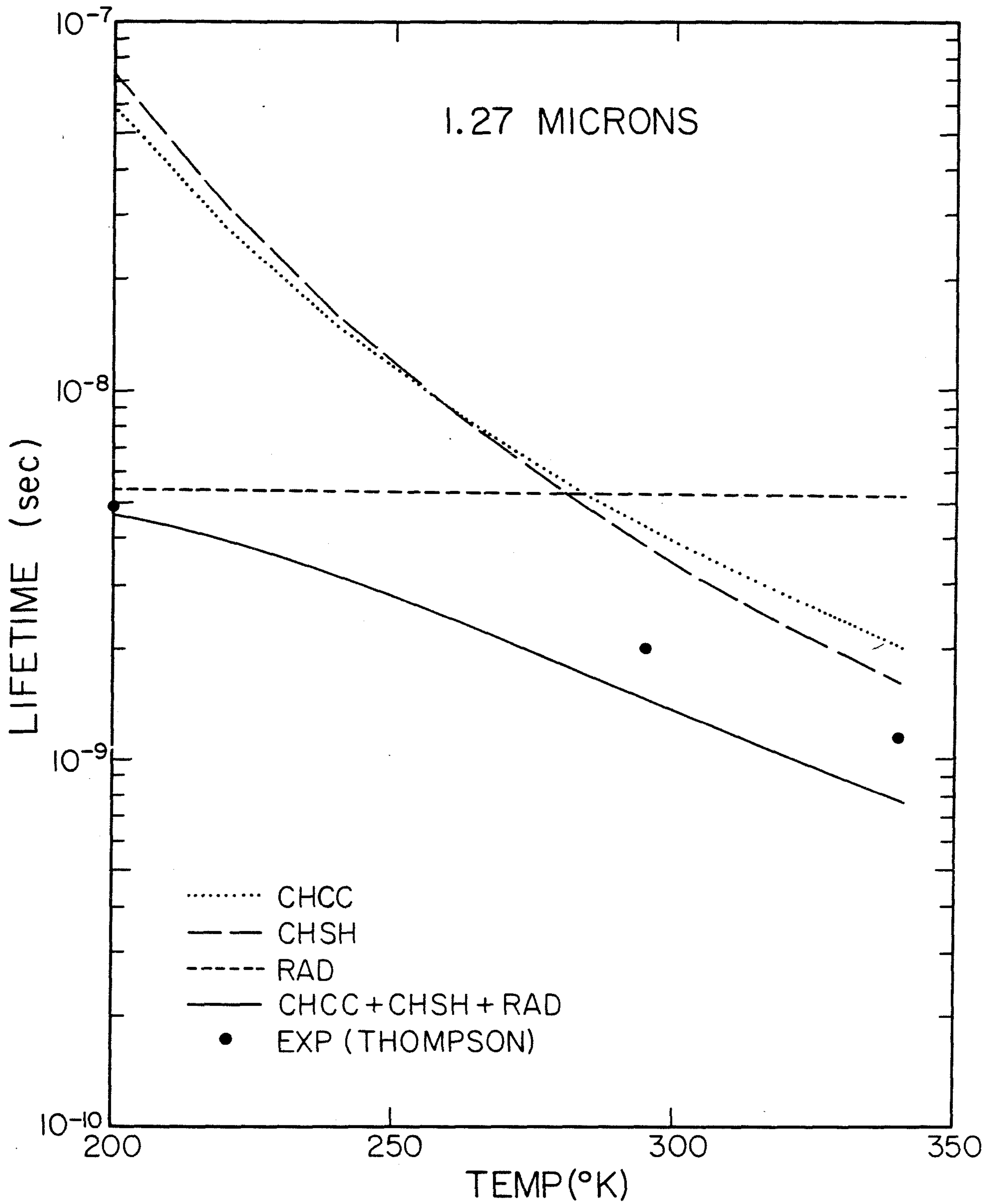

Fig. 4.5 Experimental and calculated carrier lifetimes for a 1.27 μm InGaAsP/InP laser.

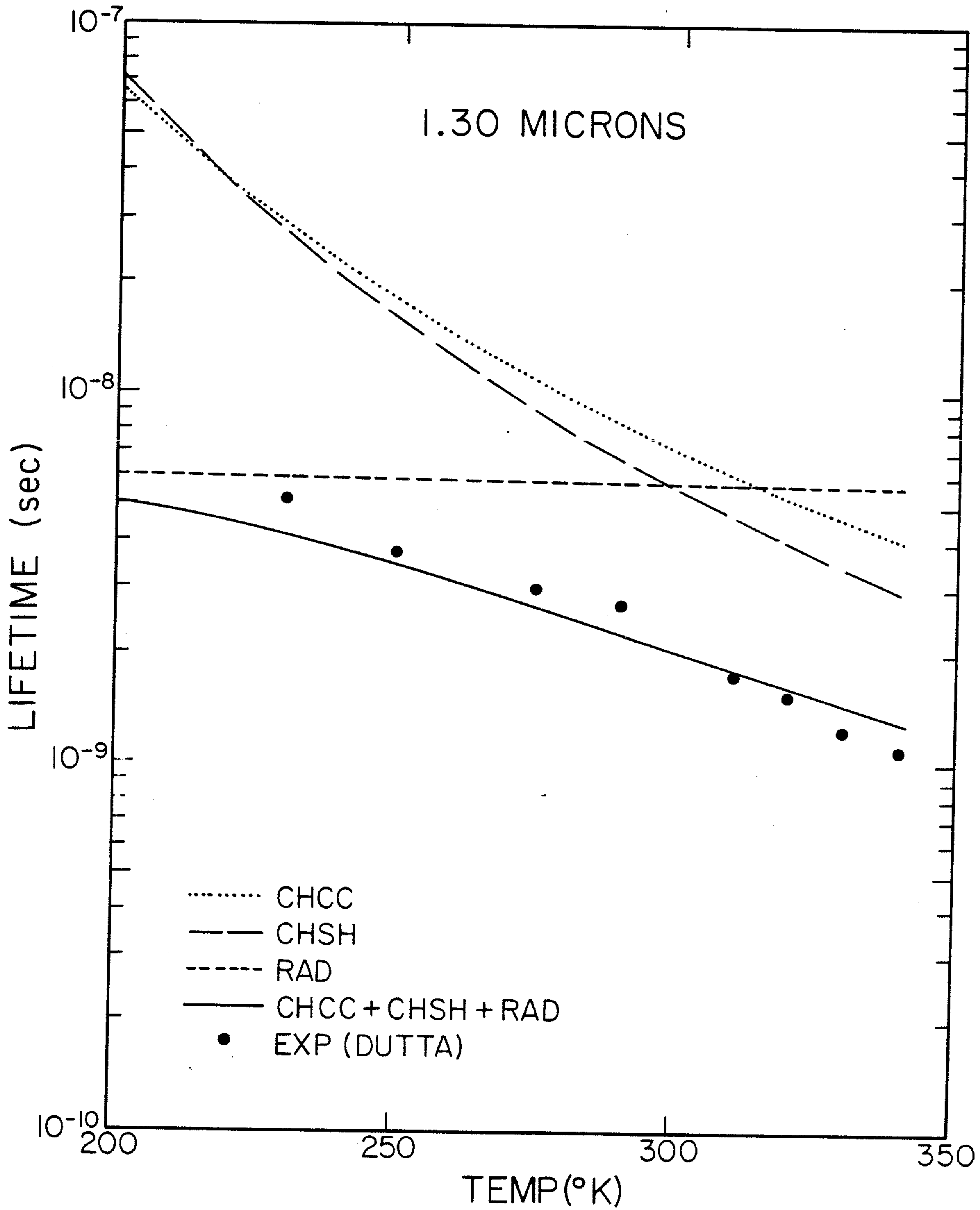

Fig. 4.6 Experimental and calculated carrier lifetimes for a 1.3 μm InGaAsP/InP laser.

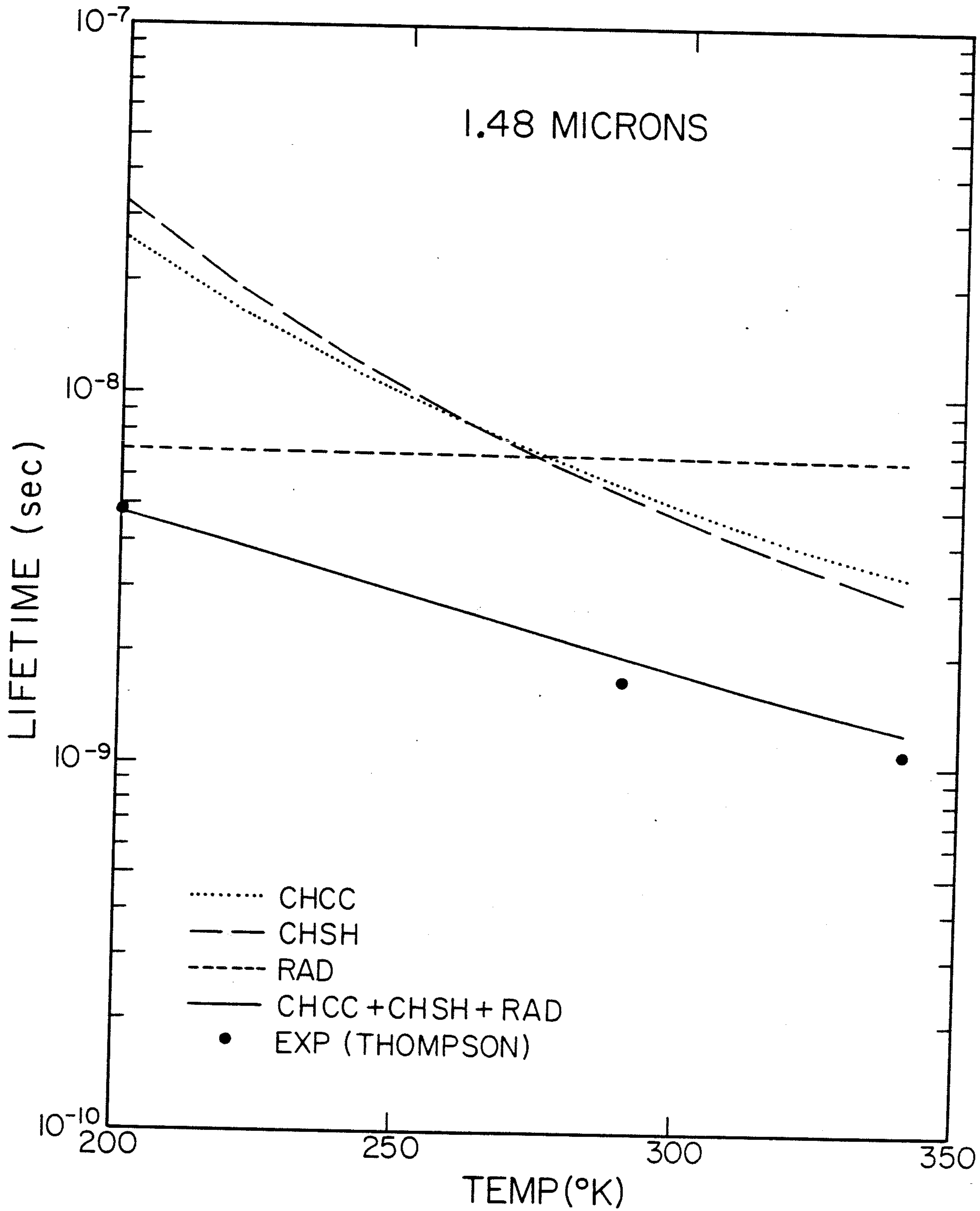

Fig. 4.7 Experimental and calculated carrier lifetimes for a 1.48 μm InGaAsP/InP laser.

mechanisms not accounted for here. Since the Auger lifetime is a rather sensitive function of carrier concentration (see Fig. 4.8), calculations are meaningful only if reliable values of n_{th} can be obtained.

It should be pointed out that the calculated non-radiative lifetime is only dependent on n_{th}, which is obtained from measured carrier lifetime and threshold current (EQ. 4.4). Therefore, agreement between calculated and measured lifetimes automatically accounts for the observed temperature dependence in the low T_o regime.

We have also examined the phonon-assisted Auger recombinations. It has been proposed that these processes are important in semiconductors at low temperatures, since the participation of a phonon relaxes the requirement of simultaneous energy and momentum conservation of the electrons and holes [18]. Our preliminary calculations show that while the Auger lifetime of phonon-assisted CHCC and CHSH processes are shorter than the normal CHCC and CHSH processes at low temperatures (< 150 °K), they are at least an order of magnitude longer above 200 °K. Therefore their contribution to the total carrier lifetime can be neglected.

The Auger lifetime is known to vary approximately with the carrier concentration as [20]

$$\frac{1}{\tau} \sim n^a \tag{4.14}$$

where a is between 2 and 4. By varying n, we have plotted calculated $\frac{1}{\tau}$ vs n for a 1.3 μm laser at 300 °K (Fig. 4.8) on a log-log scale. The slopes of the lines indicate that a=2.19 for the CHCC process and a=2.04 for the CHSH process. The combined non-radiative Auger lifetime varies with $n^{2.10}$. This compares favorably with the value of 2.2 obtained on LED experiments by Uji et al [20].

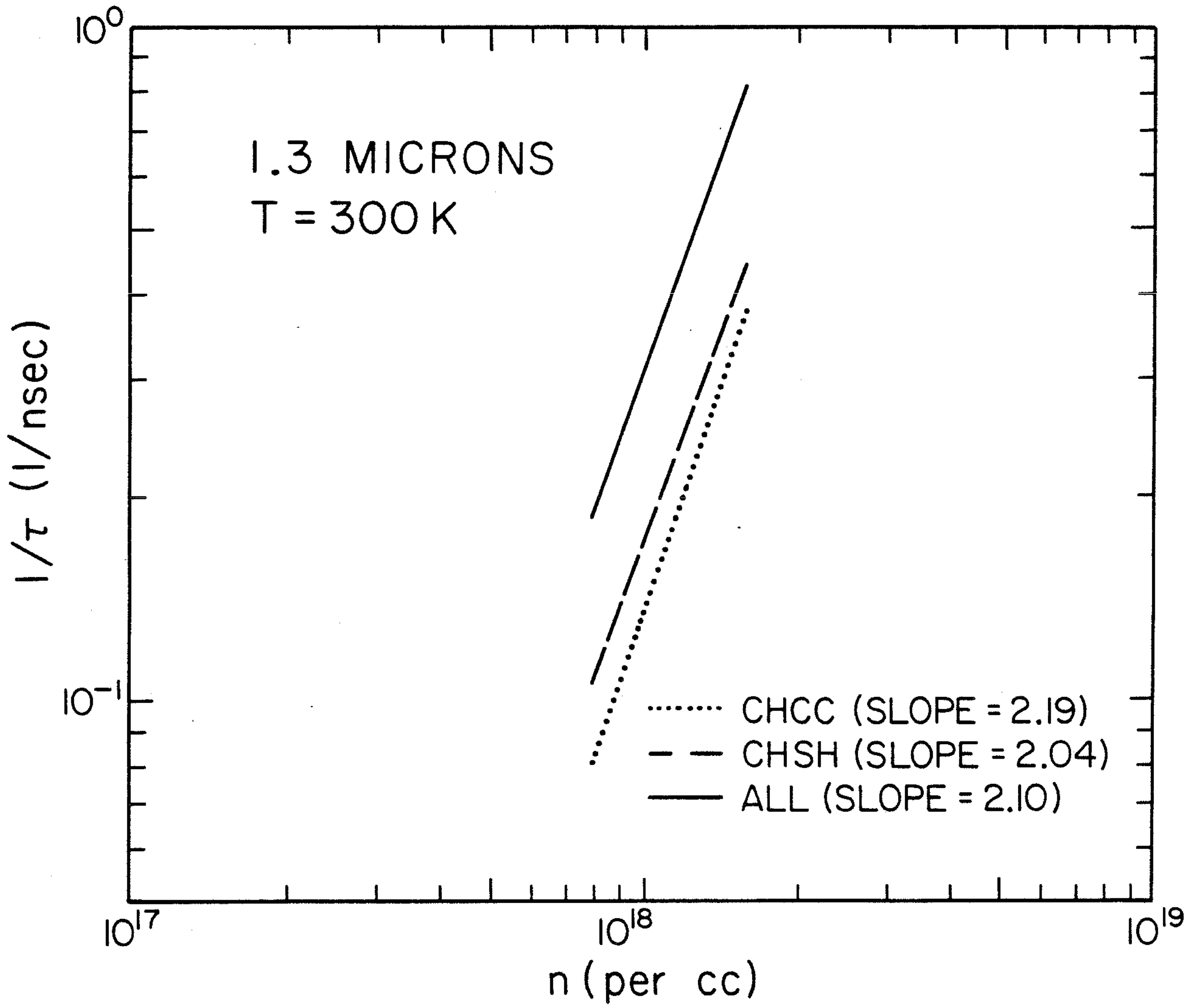

Fig. 4.8 Plot of inverse carrier lifetime vs injected carrier concentration.

The Auger lifetime for an GaInAsSb/GaAlAsSb laser emitting at 1.8 μm has also been calculated. The data for this laser are taken from ref. 21. Since limited information is available, linear interpolation is taken between the binary compounds of GaAs, InAs, and InSb to obtain the relevant parameters needed. One interesting result worth mentioning is that the lifetime for the CHSH process is about two orders of magnitude longer than the CHCC process. This we believe is due to the large Δ in this system. The calculated and experimental values are compared in Fig. 4.9, and reasonable agreement exists. However, since the band parameters used here are less accurate than those in the GaInAsP/InP system, the result presented here should only be regarded as preliminary. An interesting property of this laser is its high T_o ($\sim$ 112 °K), which may be due partially to the the absence of the CHSH process. It should be pointed out that non-radiative Auger recombination cannot explain the decrease in differential quantum efficiency in this laser [21].

In conclusion, it has been demonstrated that the Auger lifetime for both CHCC and CHSH proceses are comparable in the temperature range of 200–340 °K. Reasonable agreement was obtained for the measured and calculated lifetimes of low threshold lasers emitting from 1.1 to 1.48 μm. Results indicate that the non-radiative Auger recombination is an important factor responsible for the high temperature sensitivity of the threshold current of GaInAsP/InP quaternary lasers.

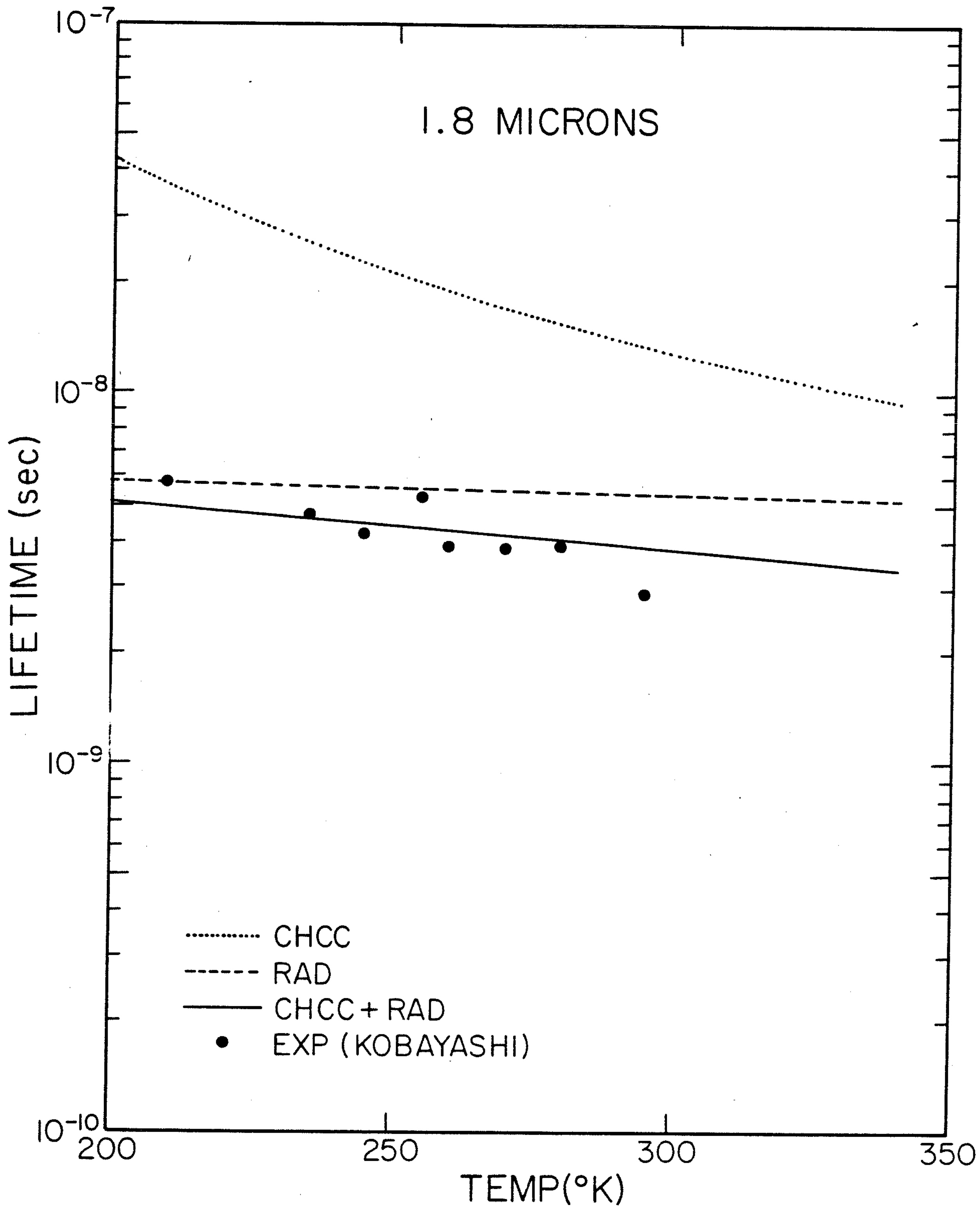

Fig. 4.9 1.8 μm GaInAsSb/GaAlAsSb laser.

References - Chapter 4

1. Y. Horikoshi and Y. Furukawa, "Temperature Sensitive Threshold Current of InGaAsP-InP Double Heterostructure Lasers," Japan. J. of Appl. Phys. **18** , 809(1979)

2. Y. Horikoshi H. Saito, M. Kawashima and T. Takanashi, "Low-Temperature Behavior of the Threshold Current and Carrier Lifetime of InGaAsP-InP DH Lasers," Japan. J. Appl. Phys. **18** , 1657(1979)

3. G. H. B. Thompson and G. Henshall, "Nonradiative Carrier Loss and Temperature Sensitivity of Threshold in 1.27 μm (GaIn)(AsP)/InP D.H. Lasers," Electron. Lett. **16** , 42(1980)

4. G. H. B. Thompson, "Temperature Dependence of Threshold Current in (GaIn)(AsP)/InP DH Lasers at 1.3 and 1.5 μm Wavelength," IEE Proc. **128** Pt. 1, 37(1981)

5. N. Dutta and R. Nelson, "Temperature Dependence of Threshold of InGaAsP/InP Double-Heterostructure Lasers and Auger Recombination," Appl. Phys. Lett. **38** , 407(1981)

6. M. Ettenberg, M. Nuege and H. Kressel, "The Temperature Dependence of Threshold Current for Double-Heterojunction Lasers," J. Appl. Phys. **50** , 2949(1979)

7. M. Asada, A Adams, K Stubkjaer, Y. Suematsu, Y Itaya and S. Arai, "The Temperature Dependence of the Threshold Current of GaInAsP/InP DH Lasers," IEEE J. Quan. Elect., **QE-17** , 611(1981)

8. A.R. Goodwin, J.R. Peters, M. Pion, G.H.B. Thompson, and J.E.A. Whiteaway, "Threshold Temperature Characteristics of Double Heterostructure $Ga_{1-x}Al_xAs$ Lasers," J. Appl. Phys. **46** , 3126(1975)

9. N.K. Dutta, R.J. Nelson, and P.A. Barnes, 'Temperature Dependence of Threshold and Electrical Characteristics of InGaAsP-InP D.H. Lasers," Electron. Lett. **16** , 653(1980)

10. A. Sugimura, 'Band-to-Band Auger Effect on the Output Power Saturation in InGaAsP LED's," IEEE J. Quan. Elect. **QE-17** , 441(1981)

11. A. R. Beattie and P. T. Landsberg, "Auger Effect in Semiconductors," Proc. R. Soc. London, Ser. A **249** 16(1958); or

    L. Huldt, "Auger Recombination in Germanium," Phys. Stat. Sol. (a) **24** , 221(1974)

12. E. Antoncik and P. T. Landsberg, "Overlap Integrals for Bloch Electrons," Proc. Phys. Soc. **82** , 337(1963)

13. M. Takeshima, "Auger Recombination in InAs, GaSb, InP, and GaAs," J. Appl. Phys. **43** , 4114(1972)

14. A. Sugimura, 'Band-to-Band Auger Recombination Effect on InGaAsP Laser Threshold," IEEE J. Quan. Elect. **QE-17** , 627(1981)

15. A. Sugimura, 'Band-to-Band Auger Effect in GaSb and InAs Lasers," J. Appl. Phys. **51** , 4405(1980)

16 N. K. Dutta, "Gain-Current Relation for $In_{0.72}G_{0.28}As_{0.6}P_{0.4}$ Lasers," J. Appl. Phys. **52** , 55(1981)

17. Y. Yamazoe, T. Nishino and Y. Hamakawa, 'Electroreflectance Study of GaInAsP Quaternary Alloys Lattice Matched to InP," IEEE J. Quan. Elect. **QE-17** , 139(1981)

18. J. J. Hsieh and C. C. Shen, 'Room Temperature CW Operation of Buried-Stripe Double-Heterostructure GaInAsP/InP Diode Lasers," Appl. Phys. Lett. **30** , 429(1977)

19. A. Haug, 'Phonon-Assisted Auger Recombination in Degenerate Semiconductors," Sol. State Comm. **22** , 537(1977) and references therein.

20. T. Uji, K. Iwanoto and R Lang, 'Nonradiative Recombination in InGaAsP/InP Light Sources Causing Light Emitting Diode Saturation and Strong Laser-Threshold-Current Temperature Sensitivity," Appl. Phys. Lett. **38** , 193(1981)

21. N. Kobayashi, Y. Horikoshi and C. Uemura, 'Room Temperature Operation of the InGaAsSb/AlGaAsSb DH Laser at 1.8 μm Wavelength," Japan. J. Appl. Phys. **19** , L30(1980)

Chapter 5

Some Growth and Processing Techniques of GaInAsP/InP Devices

5.1 Introduction

Throughout the course of this thesis research program, heavy reliance on proper device fabrication techniques is required. The most basic and crucial aspect is, of course, the epitaxy of successive layers of InP and quaternary GaInAsP crystals onto a given InP substrate. In our laboratory, these wafers are grown by liquid phase epitaxy (LPE). In this chapter, details of the growth will be described, as will other important processing techniques.

5.2 LPE of GaInAsP/InP Materials

Although in the GaAlAs/GaAs system, other means of growth, such as molecular beam epitaxy (MBE) [1,2], and metalorganic chemical vapor deposition (MO-CVD) [3], have advanced to a stage where better uniformity and growth morphology than LPE can be achieved, these techniques are still under examination for the quaternary GaInAsP system. Some workers in the field have grown device quality wafers by both halide-transport CVD [4] and MO-CVD [5], but there are still insufficient data available to make justifiable comparisons with LPE grown devices.

In our LPE growths, we have employed the standard sliding boat technology. The boat, made from high quality purified graphite (MFB-3-2 from Pogo Graphite), consists of three parts, a body, a slider with a recessed bin that carries the substrate wafer, and a top piece with multiple slots which contains the growth solutions. The schematic of the boat is shown in Fig. 5.1. The growth system, shown in Fig. 5.2, consists primarily of a three-zone furnace, a palladium purified hydrogen source, and a quartz tube growth chamber. The

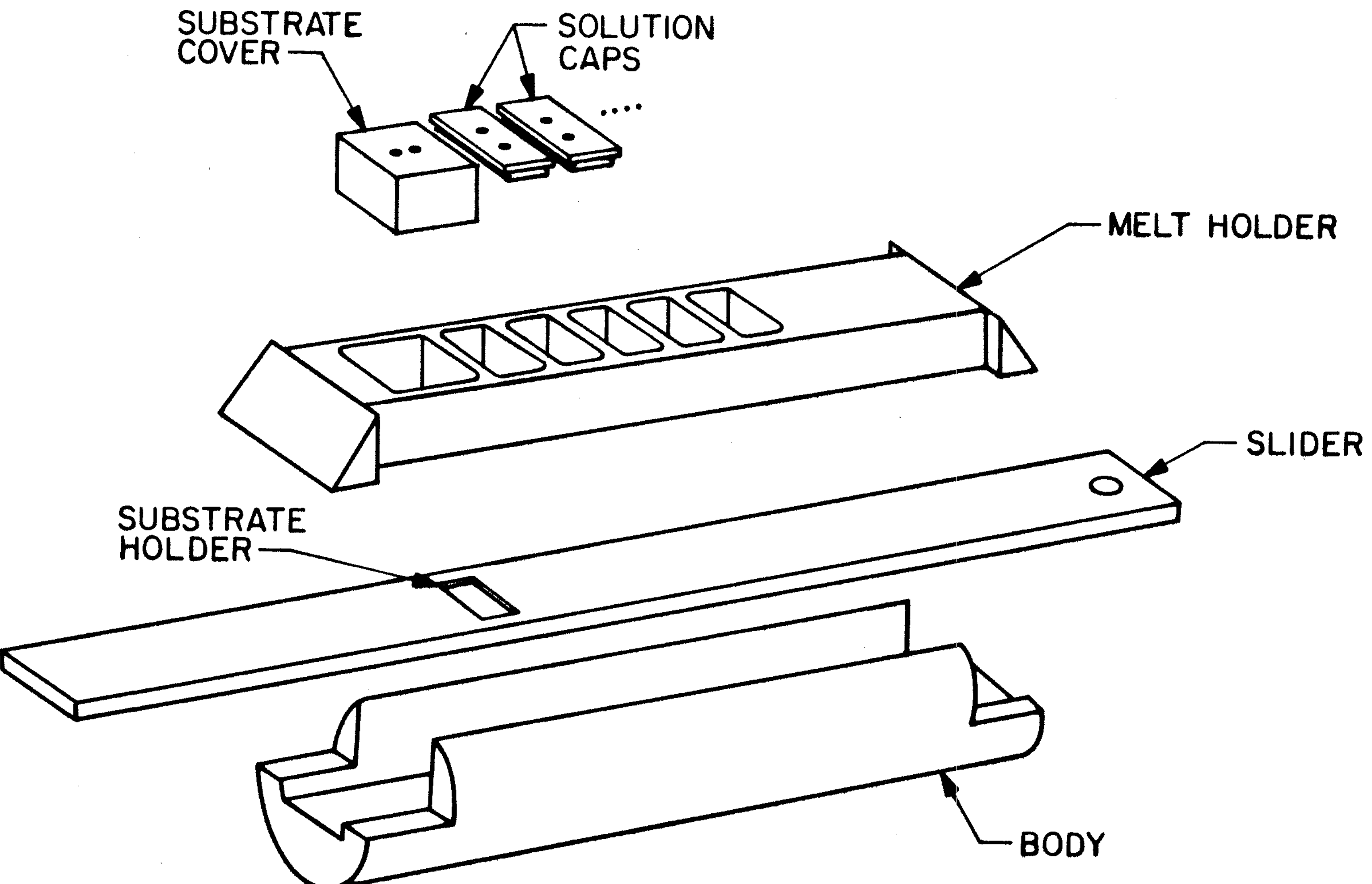

Fig. 5.1 Schematic of graphite boat used in LPE growth of GaInAsP/InP.

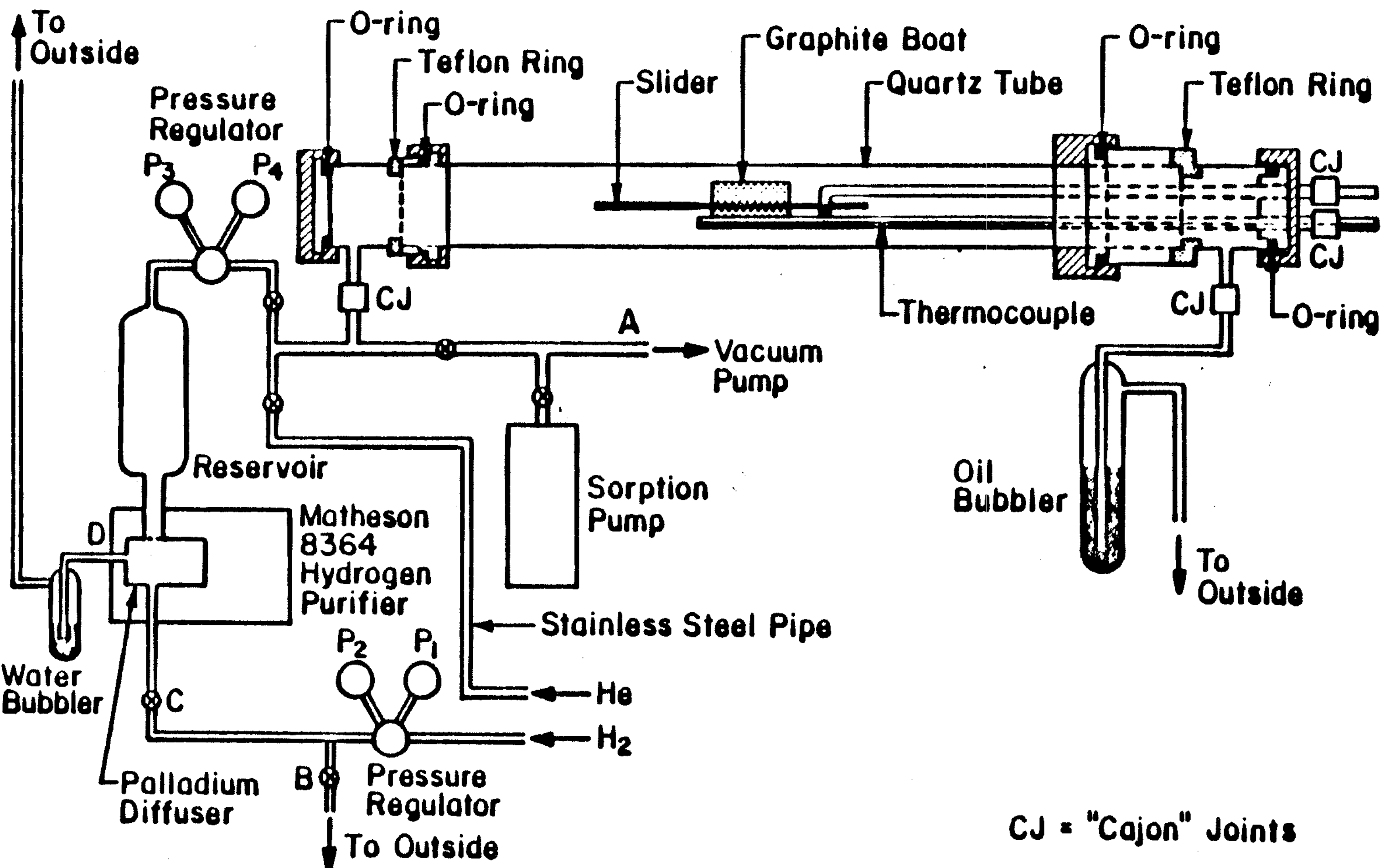

Fig. 5.2 Schematic of growth system.

graphite boat sits on a quartz holder inside the growth chamber while the slider is moved via a glass rod attachment.

At present, a few methods of growth of the GaInAsP/InP structures by LPE are available. These include the step-cooled growth [6], near-equilibrium growth [7] and the two-phase growth [8,9]. The step-cooled growth is described in chapter 3. Basically, an exact amount of phosphorus, usually in the form of crystalline InP, is added to saturate a solution of In (or In-Ga-As in the case of a quaternary melt) at temperature T_o. The temperature of the system is lowered to T_1 before the substrate is brought into contact with the solution. Thus the epilayer is grown with a solution supercooling of amount $\Delta = T_o - T_1$. (Fig. 3.4) Near equilibrium growth is similar, but Δ is kept to be almost zero, and the system is cooled at a fixed rate to grow the layer. Two phase growth does not require an exact quantity of phosphorus to be added. Instead, an excess amount of InP is added so that some remaining InP floats on the top of the solution. After the melts have reached equilibrium at the initial temperature, a cooling rate is established in the system. Due to the finite diffusivity of phosphorus molecules in the solution, the bottom of the solution will be supercooled with respect to the top, where the floating InP pieces have kept it at equilibrium. This method is simpler to use because exact knowledge of the liquidus temperature of the melt is not needed (this temperature is difficult to determine without a transparent furnace).

The two phase growth, as well as any other which grows the layers with a temperature ramp, does not produce thick quaternary layers with uniform composition due to the temperature dependent distribution coefficients of the various components [10]. Compositional grading is accompanied by lattice mismatch which cannot be tolerated in high performance optical devices. However, for growing less than one μm layers, as is typical in semiconductor laser active

layers, the grading is minimal and this method has been successful.

In a typical run, 99.9999% (six 9's) pure indium pellets are placed in the graphite boat solution slots and baked at 730 °C for about ten hours in a palladium-purified hydrogen atmosphere within the quartz reactor tube. After this, the (100) InP substrate, dopants and source wafers are loaded. The source wafers consist of measured amounts of GaAs, InAs and excess (100) InP for the quaternary melt, and polycrystalline InP for the InP melts. The cleaning procedure for these materials is described in the appendix. The reactor is flushed with hydrogen for several hours, or until the oxygen level falls to a few tenths of one ppm. The temperature is then increased to 675 °C, and held there for one hour while the In-P and Ga-In-As-P solutions become saturated from the floating InP.

It is a well-known fact that InP dissociates at temperatures above 450 °C. The loss of phosphorus by evaporation leaves a pitted surface unsuitable for growth. To alleviate this problem, a large InP wafer is usually employed as a cover over the substrate bin. An additional graphite weight is placed on top of this wafer. This configuration provides a high phosphorus pressure over the substrate to suppress thermal decomposition. As a further precaution, the substrate is passed under an undersaturated indium melt to etch off the damaged surface.

After the saturation step, a cooling rate of 0.7 °C/min is established in the system. Then successive epi-layers are deposited by sliding the substrate under each melt. The quaternary layer is usually grown at 635 °C as indicated by a chromel-alumel thermocouple placed under the graphite boat. Data from reference 6 are used for growth of the quaternary layer. The melt composition is varied slightly to account for system variances so that lattice matched layers on InP can be grown, as verified by X-ray diffraction measurements. It is found that monitoring of the absolute temperature of growth is rather crucial for

consistent growth of lattice matched material. This is probably due to temperature dependent distribution coefficients of the various solution components [11]. When lattice mismatch is large, incomplete melt wipeoff is usually observed. The crystal surface morphology will also exhibit cross-hatched patterns rather than the smooth, terraced appearance typical of good growths.

Doping of the InP layers is accomplished by adding a measured amount of the appropriate element. For n-type layers, five 9's or six 9's purity tellurium or tin is used, whereas zinc is the only common dopant for p-type materials. The doping ability of each of these elements is shown is Fig. 5.3 for growths occurring at around 640 °C from ref 12. The distribution coefficient, defined as $k = \frac{[A]_{solid}}{[A]_{liquid}}$, where [A] is the mole fraction of element A, is very high for Te and Zn. In the case of Zn, the doping level saturates at around $2x10^{18}cm^{-3}$.

The use of zinc as a dopant poses some problems. Its high vapor pressure and high distribution coefficient causes contamination of other melts. Furthermore, during growth of the p-layer, zinc diffuses into the underlying layer. Lasers with such misplaced junctions have significantly higher thresholds and lower quantum efficiencies [13]. To overcome these problems, the zinc concentration in the melt must be reduced. The minute quantity of zinc needed for doping is provided by a Zn-In alloy. In addition, graphite caps are employed over all the solution slots to contain the zinc vapor.

5.3 Device Processing

In this section, procedures leading to the completed CW oxide stripe laser will be described to illustrate the necessary processing steps.

First, four layers, InP ($n \sim 10^{18}$), quaternary GaInAsP (unintentionally doped), InP ($p \sim 7x10^{17}$) and quaternary GaInAsP ($p \sim 2x10^{18}$) are successively grown. The

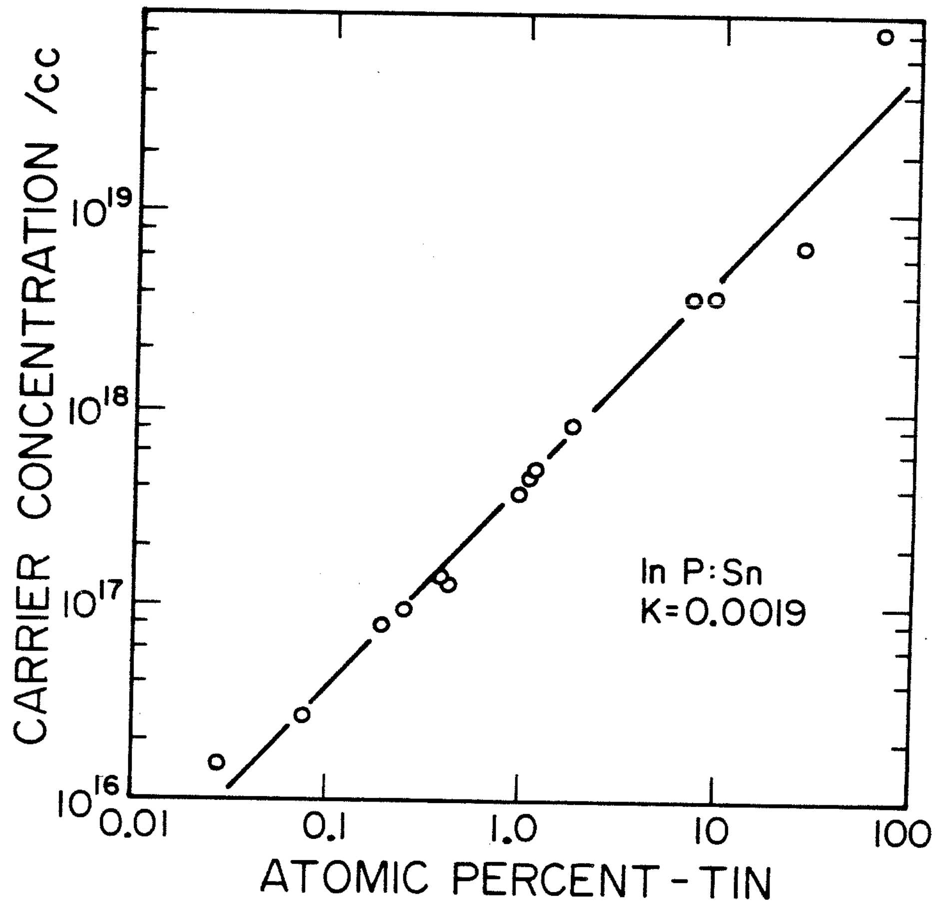

Fig. 5.3 a) doping of LPE InP with Tin

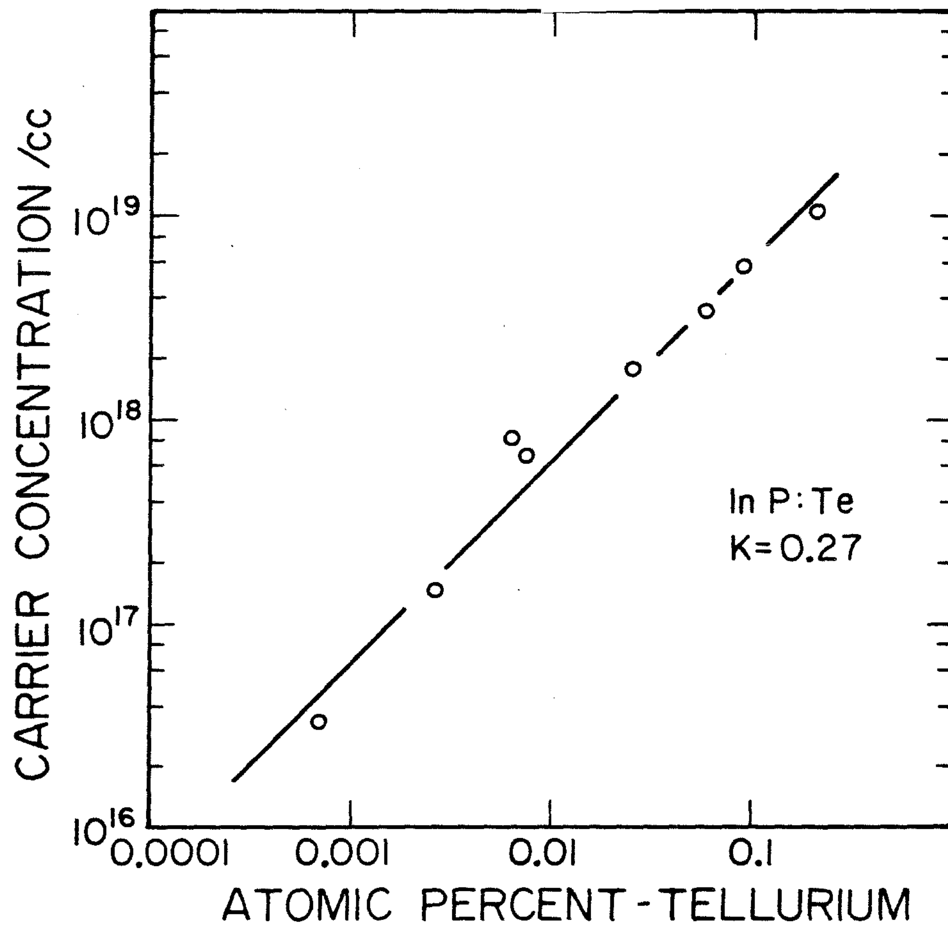

Fig. 5.3 b) doping of LPE InP with Tellurium

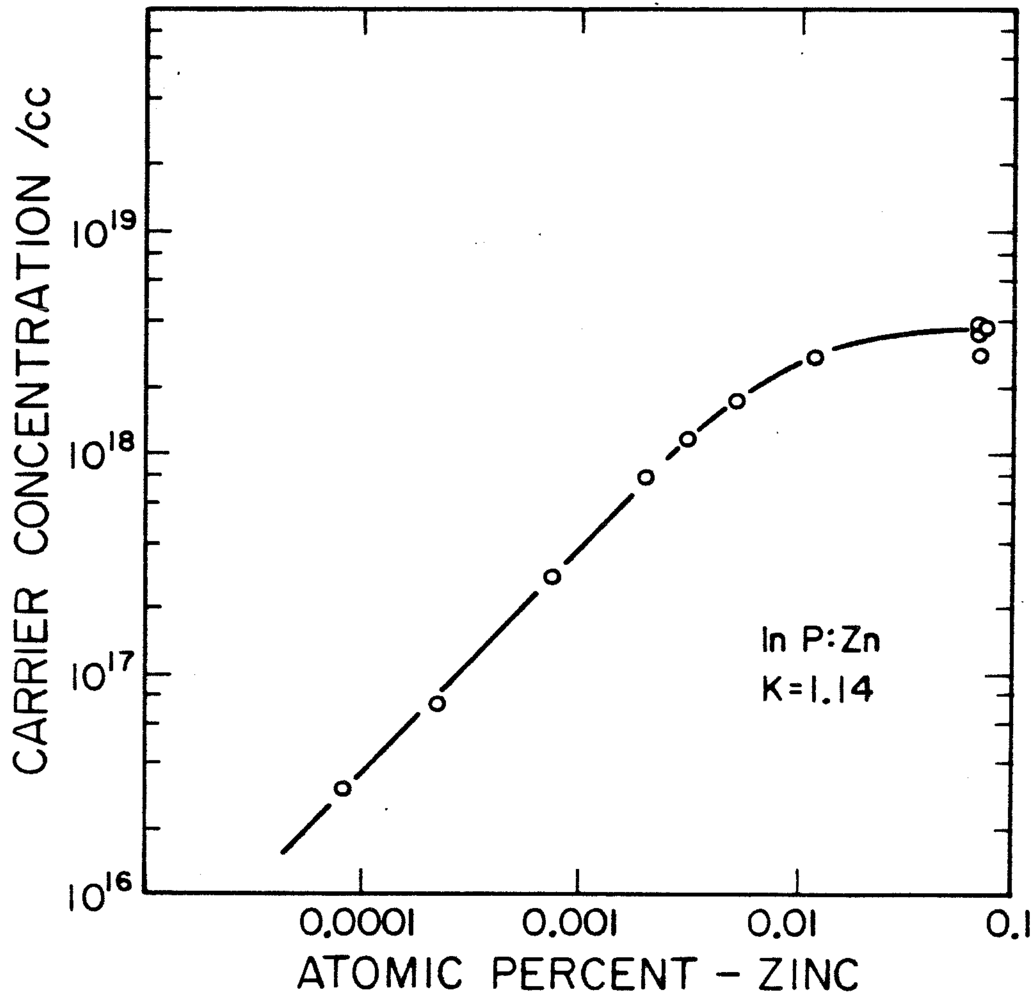

Fig. 5.3 c) doping of LPE InP with Zinc

respective thicknesses are 5, 0.3, 2 and 1 μ. The bottom buffer layer provides a smooth growth surface for the quaternary active layer after the indium etch. Growth of the additional 1 μm quaternary cap layer gives rise to a low contact resistance crucial for CW operation since p-doped InP typically has much higher contact resistance [14]. After growth, any excess indium is melted by heating and wiped off the wafer surface with a Q-tip dipped in methanol. Any remaining trace indium droplets are removed by soaking in hydrochloric acid for thirty seconds. HCl attacks InP and indium but does not affect the top quaternary layer which protects the underlying layers.

Following the cleaning step, the wafer is coated with 2000Å of silicon nitride or silicon dioxide in the chamber described in the appendix. The coated wafer is treated with Resist-Aid (Transene Co.) to improve photoresist adhesion to the dielectric. Shipley 1350J resist is spun on at 5000 rpm and prebaked under an infra-red lamp for five minutes. Periodic 15 μ wide stripes, aligned at right angles to one of the natural cleavage planes of the (100) wafer, are selectively exposed through a mask by a UV lamp. After developing, the photoresist is baked at 90 °C for thirty minutes. The resulting pattern acts as an etch mask for the underlying dielectric layer. In this way, 15 μ wide lines of the quaternary cap layer are exposed from the dielectric with an etch in buffered-HF. About thirty seconds are needed to etch away silicon dioxide, while roughly four minutes are needed if the dielectric is silicon nitride.

Au-Zn (5% Zn by weight) is evaporated over the top surface and the contact is alloyed at 420 °C for thirty seconds. The wafer is then lapped down on the substrate side to 75 μm. Next, Au-Ge (eutectic mixture) is evaporated onto the wafer bottom and alloyed at 250 °C for two minutes to form the n-contact. The wafer is cleaved perpendicular to the stripes and diced into individual chips 300 μm in length. These are now ready to be bonded down to heat sinks. The above

steps are illustrated in Fig. 5.4.

The heat sinks are copper blocks tin plated to a thickness of several μm. A little flux is spread over the tin surface and the laser chip is placed on it with the stripe side down. Some weight, provided by a glass slide, is placed over the wafer to improve contact and provide pressure between the surfaces. The entire assembly is then heated to about 230 °C (near the melting point of tin) to effect bonding between tin and gold surfaces. The completed block is dipped in acetone to clean off excess flux, and prepared for measurements of pulsed and CW thresholds. Using this procedure, we have been able to obtain lasers with pulsed thresholds of 200 mA and CW thresholds of 300 mA. The difference between pulsed and CW thresholds is still rather large because the device series resistance of 6-8 ohms is still not optimized.

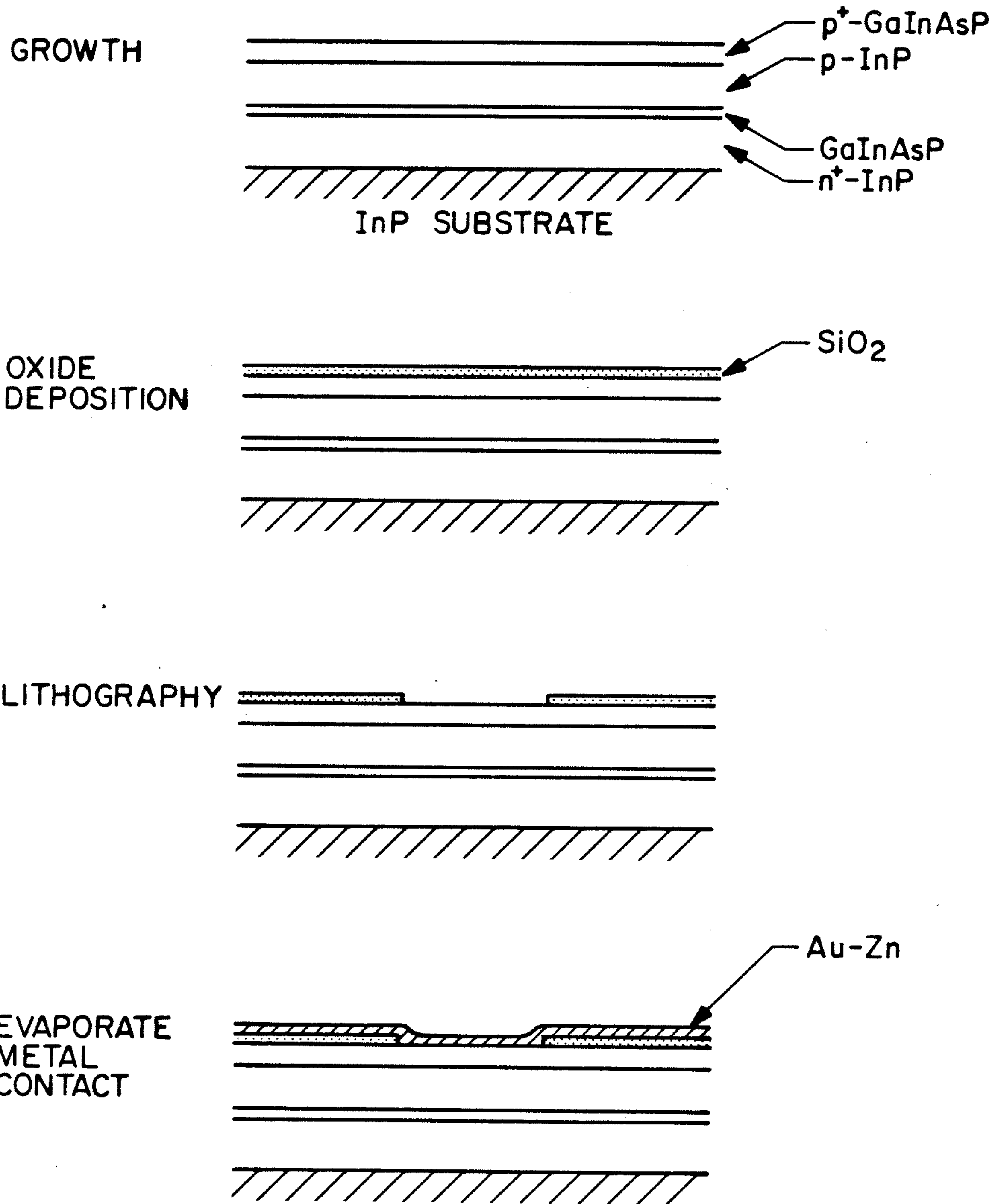

Fig. 5.4 Processing steps for Oxide Stripe lasers.

Appendix A: Cleaning and Etching Precedures

Indium pellets for the melt are etched in concentrated nitric acid for about two minutes, then rinsed in de-ionized (DI) water, followed by spectroscopic grade methanol. They are then blown dry and immediately loaded into the boat for baking.

Preparation of the wafer for growth requires meticulous attention. The polished InP substrate is first degreased in acetone, followed by methanol and then rinsed in de-ionized (DI) water. A soak in concentrated nitric acid of three to five minutes seems to result in a smoother surface in the ensuing etch. After rinsing in DI water, the wafer is placed in 1% Br-Methanol for several minutes to remove the top surface which is damaged during mechanical polishing. Then it is rinsed in methanol, DI water and blown dry with a nitrogen jet.

Polycrystalline GaAs and InAs for the quaternary melt are cleaned by etching in 5% Br-Methanol for ten minutes. Similarly, polycrystalline InP source pieces are etched in concentrated hydrochloric acid for one minute. These are then rinsed and blown dry.

Appendix B: The Silicon Nitride Deposition System

During the course of this research, good quality insulating dielectric films were often necessary. Towards this end, a silicon nitride CVD deposition system was designed and built. Fig. 5.5 shows a schematic of the setup. 5% silane in nitrogen, electronic grade ammonia and carrier gas nitrogen were mixed just prior to entry into the deposition chamber. The deposition takes place on a thin graphite heater strip which has a series of holes drilled on either side of the sample area to ensure more uniform current and to reduce heat loss through to ends of the strip. The ability to heat up the sample rapidly is not only crucial for good quality layers. but also crucial in minimizing thermal damage of InP wafers during this process. Silane is only introduced into the chamber after prolonged flushing with nitrogen because silane reacts with trace oxygen even at room temperature. Then, flowrates of 500 scc/min of the 5% silane in nitrogen, 750 scc/min of nitrogen and 1000 scc/min of ammonia are established. After several minutes when the mixture of ammonia, silane and carrier gases has stabilized inside the growth chamber, the graphite strip is heated rapidly to 700 °C. Formation of silicon nitride is evidenced by observing the interference color of the deposited film. Typically, 1000Å is deposited in about thirty seconds.

The mechanical quality and adhesion of the dielectric grown by this method is excellent. We have applied this film as a diffusion mask against zinc and also as a growth mask in the processing of embedded lasers with considerable success.

We are grateful to Dr. J.P. Donnely of Lincoln Labs for precious suggestions and assistance in the designing of this system.

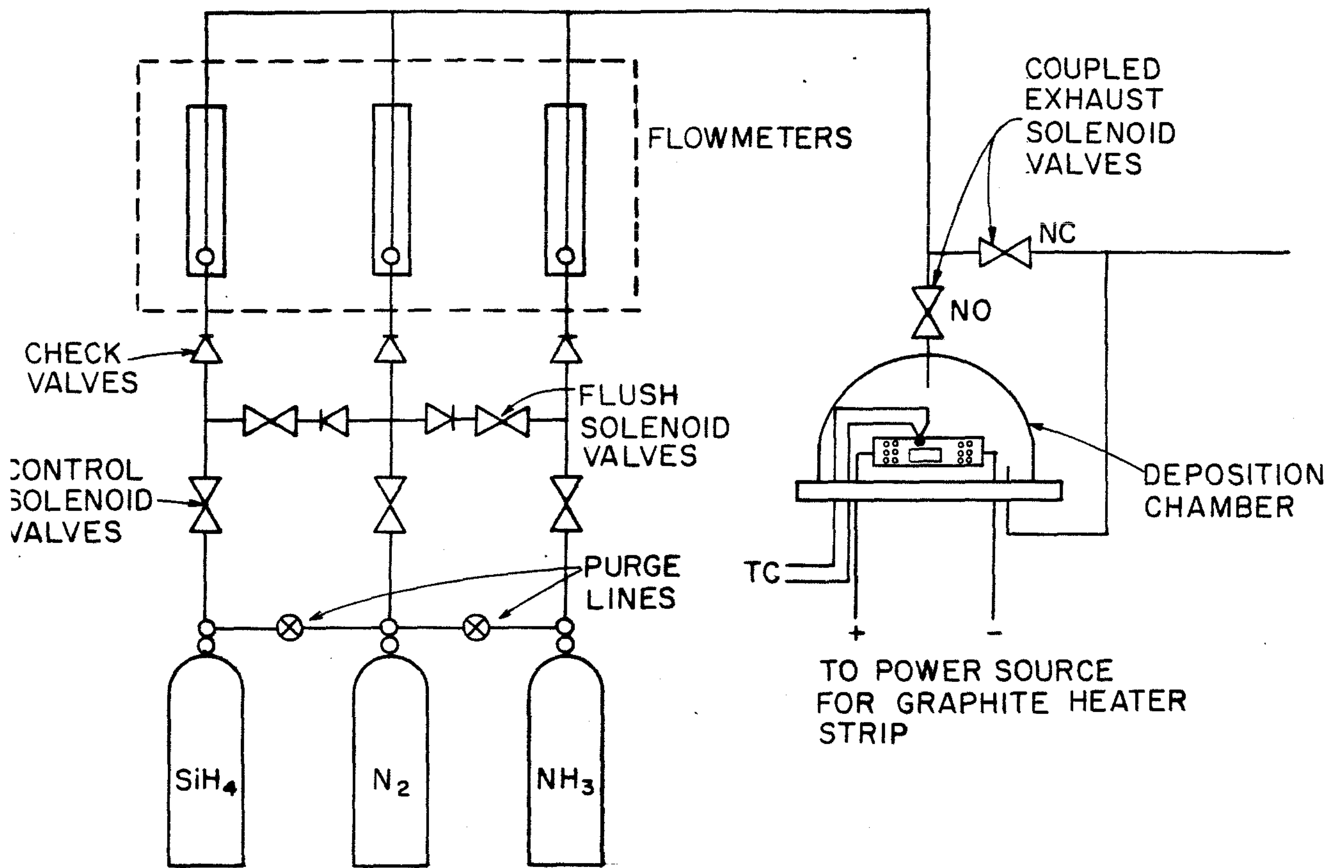

Fig. 5.5 Schematic of Silicon Nitride Deposition System.

References - Chapter 5

1. A. Y. Cho, R. W. Dixon, H. C. Casey Jr., and R. L. Hartman, "Continuous Room-Temperature Operation of GaAs-GaAlAs Double-Heterostructure Lasers prepared by Molecular-Beam Epitaxy," Appl. Phys. Lett. **28** , 501(1976)

2. W. T. Tsang, "High-Through-Put, High-Yield, and Highly-Reproducible (AlGa)As Double-Heterostructure Laser Wafers Grown by Molecular Beam Epitaxy," Appl. Phys. Lett. **38** , 587(1981)

3. R. D. Dupuis and P. D. Dapkus, "Very Low Threshold $Ga_{1-x}Al_xAs$-GaAs Double-Heterosturcture Lasers Grown by Metalorganic Chemical Vapor Deposition," Appl. Phys. Lett. **32** , 473(1977)

4. G. H. Olsen, C. J. Nuese and M. Ettenberg, "Low-Threshold 1.25 μm Vapor-Grown InGaAsP CW Lasers," Appl. Phys. Lett. **34** , 262(1979)

5. J. P. Hirtz and J. P. Duchemin, "Organometallic Growth of Device Quality GaInAs and GaInAsP on InP by Cracking of $In(C_2H_5)_3$," Paper **H-1** , Electronic Materials Conf., June 24-25, 1980, Ithaca, N.Y.

6. M. Feng, T. H. Windhorn, M. J. Tashima and G. E. Stillman, "Liquid-Phase Epitaxial Growth of Lattice-Matched InGaAsP on (100)-InP for the 1.15-1.31 μm Spectral Region," Appl. Phys. Lett. **32** , 758(1978)

7. R. J. Nelson, "Near-Equilibrium LPE Growth of Low Threshold Current Density $In_{1-x}Ga_xAs_yP_{1-y}$ (λ=1.35μm) DH Lasers," Appl. Phys. Lett. **35** , 654(1979)

8. K. Sakai, S. Akiba, and T. Yamamoto, "Growth of Lattice-Matched InGaAsP/InP Double-Heterosturctures by the Two-Phase Supercooled Solution Technique," Japan. J. Appl. Phys. **16** , 2043(1977)

9. M. A. Pollack, R. E. Nahory, J. C. DeWinter, and A. A. Ballman, "Liquid-Phase Epitaxial $In_{1-x}Ga_xAs_yP_{1-y}$ Lattice-Matched to <100> InP over the Complete

Wavelength 0.92 $\leq \lambda \leq$ 1.65μm," Appl. Phys. Lett. **33**, 314(1978)

10. M. Feng, L. W. Cook, M. M. Tashima, T. H. Windhorn, and G. E. Stillman, "The Influence of LPE Growth Techniques on the Alloy Composition of InGaAsP," Appl. Phys. Lett. **34**, 292((1979)

11. J. J. Coleman, "Arsenic and Gallium Distribution Coefficients in Liquid-Phase Epitaxial $Ga_xIn_{1-x}P_yAs_{1-y}$," Appl. Phys. Lett. **32**, 388(1978)

12. M. G. Astles, F. G. H. Smith, and E. W. Williams, "Indium Phosphide II. Liquid Epitaxial Growth," J. Electrochem. Soc. **120**, 1750(1973)

13. J. J. Coleman and F. R. Nash, "Zinc Contamination and Misplaced P-N Junctions in InP-GaInAsP D.H. Lasers," Electron. Lett. **14**, 558(1978)